Journal of Computational Applied Mechanics 2026, 57(3): 443-472

DOI: 10.22059/jcamech.2026.411829.1797

RESEARCH PAPER

Numerical Simulation and Visualization of Newtonian and Non-Newtonian Hemodynamics in a Stenotic Blood Vessel

Taiba Hussain [a], Osman Anwar Bég [a], Sireetorn Kuharat [a], Tasveer Anwar Bég [b], Muhammad Mubashir Bhatti [c,d,*]

[a] *MPESG, Corrosion Lab, 3-08, Aeronautical and Mechanical Engineering Division, University of Salford, M5 4WT, UK*

[b] *Engineering Mechanics Research, Israfil House, Dickenson Rd., Manchester, M13, UK*

[c] *Department of Physics, College of Science, Korea University, 145 Anam-ro, Seongbuk-gu, Seoul 02841, Republic of Korea*

[d] *Material Science Innovation and Modelling (MaSIM) Research Focus Area, North-West University (Mafikeng Campus), Private Bag X2046, Mmabatho 2735, South Africa*

Abstract

Cardiovascular disease (CVD) remains the leading cause of mortality worldwide, with atherosclerosis-driven stenoses significantly altering hemodynamic and influencing potential nanoparticle drug delivery outcomes. This study applies computational fluid dynamics (CFD) via ANSYS FLUENT finite volume software, to two-dimensional stenosed arteries of varying severities (30%, 50%, 70%) and shoulder lengths (2, 4, 6 mm). Two regimes have been compared: a steady Newtonian baseline, where viscosity and velocity remain constant and a physiologically realistic pulsatile non-Newtonian Carreau regime incorporating shear-thinning viscosity and cardiac-cycle effects. In the steady Newtonian simulations, velocity plots showed that increasing stenosis severity amplified throat jet velocities and extended recirculation zones, while shoulder length governed the sharpness and spatial extent of disturbed flow. The pulsatile Carreau model revealed systolic acceleration and diastolic deceleration in velocity contour plots, greater pressure drops with stenosis severity. It also showed wall shear stress (WSS) distributions characterized by high shear at stenotic throats and low or oscillatory shear effects downstream. These disturbed, low-WSS regions were identified as potential nanoparticle deposition sites for pharmacodynamics treatments, aligning with prior findings on plaque-prone hemodynamics. The results demonstrate that stenosis severity amplifies hemodynamic disturbances, while shoulder length shapes their distribution, together influencing the likelihood of nanoparticle residence and deposition. These findings are consistent with published literature, supporting CFD as a predictive tool for assessing hemodynamics. Future

* Corresponding author.
E-mail address: mmbhatti@korea.ac.kr

research could integrate deformable arterial walls through fluid–structure interaction (FSI), patient-specific geometries, and explicit nanoparticle transport for drug delivery in clinical translation.

Keywords: Hemodynamics; ANSYS FLUENT; atherosclerosis-driven stenoses; shoulder length shapes; cardiac-cycle effects; throat jet velocities; recirculation zones; wall shear stress (WSS).

1. Introduction

CVDs remain the leading cause of mortality worldwide, accounting for an estimated 19.8 million deaths in 2022, which represents approximately 32% of all global deaths. Of these, 85% were attributed to heart attack and stroke, as emphasized by the World Health Organization [1]. Atherosclerosis, the principal underlying cause of CVD, is characterised as a chronic inflammatory disorder in which immune-competent cells within arterial lesions produce predominantly pro-inflammatory cytokines, as noted by Frostegard [2]. The major direct cause of cardiovascular events is often the rupture of atherosclerotic plaques, which destabilises the vessel wall and precipitates acute complications. Plaque development arises from a series of complex interactions between vascular and immune cells. Ramji et al. [3] describe how endothelial cells, smooth muscle cells, and immune cells such as monocytes and macrophages contribute to this process. Hemodynamic factors play a crucial role in plaque localisation: Franck et al. [4] demonstrated that vulnerable endothelial regions frequently occur in sites of disturbed or turbulent flow, particularly at arterial bifurcations, where excessive hemodynamic stress accelerates disease progression. Similarly, Owais et al. [5] reported that arterial bends exacerbate hemodynamic disturbances, thereby increasing pathological wall loading and promoting atherosclerotic changes. This is illustrated in Figure 1, which contrasts a normal artery with one narrowed by atherosclerotic plaque, highlighting how plaque build-up alters blood flow patterns.

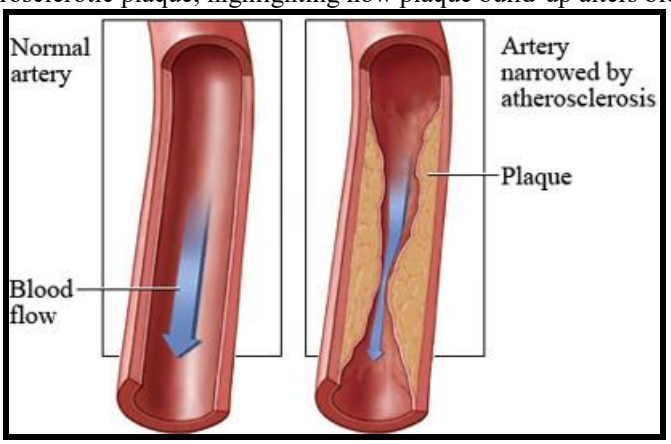

Fig 1: Normal artery VS artery with plaque build-up displaying how blood flow is affected

Hemodynamics, the study of blood flow and the forces it exerts within the circulatory system, is a central determinant of vascular health and disease, as described by Berger & Jou [6]. Key hemodynamic parameters include wall shear stress (WSS), pressure gradients, and the formation of recirculation zones downstream of stenoses or bifurcations, as noted by Nichols et al. [7]. These are not merely mechanical by-products of circulation; they have direct biological consequences for endothelial function and arterial remodelling. For instance, regions exposed to low or oscillatory WSS are strongly associated with the initiation and progression of atherosclerotic plaques, whereas high shear stress has been linked to plaque erosion or rupture as emphasized by Ku et al. [8] and Franck et al. [4]. Accurate modelling of blood rheology is essential for predicting flow behaviour and nanoparticle transport in the arterial system. While blood is a complex suspension of plasma and cellular components, it is often approximated as a Newtonian fluid in computational studies. Under this assumption, viscosity is treated as constant, with a commonly used high shear rate value of approximately 0.003-0.0035 Pa·s, corresponding to shear rates above 100 s^{-1} typical of medium to large arteries in accordance with Shibeshi & Collins [9] and Johnston et al. [10]. This simplification is computationally efficient and has been shown to reasonably capture bulk flow characteristics such as velocity and pressure distributions as highlighted by Ballyk et al. [11] and Morbiducci et al. [12]. However, blood is in fact a shear-thinning fluid, meaning its apparent viscosity decreases with increasing shear rate. This non-Newtonian behaviour becomes especially important in low-shear environments, such as those described by Zaman et al. [13] and Vasu et al. [14]. This is further supported by Cho & Kensey [15] wherein it is shown that non-Newtonian behaviour becomes especially important in post-stenotic recirculation zones, bifurcations, or regions

adjacent to atherosclerotic plaques. In such disturbed flow regions, Newtonian models often overpredict wall shear stress (WSS) compared to non-Newtonian formulations [10]. They may also underestimate flow separation and recirculation zones, features strongly associated with plaque progression, thrombosis, and nanoparticle deposition [11, 12]. To address these limitations, non-Newtonian models such as the Carreau-Yasuda formulation are widely adopted. This model represents viscosity as a function of shear rate, enabling a smooth transition between Newtonian-like behaviour at low shear rates and power-law behaviour at high shear rates, as noted by Nader et al. [16]. Mandal [17] emphasized that non-Newtonian effects are appreciable primarily in small vessels or low-shear conditions, while the Newtonian approximation remains valid in larger arteries. While arterial location is a key determinant of disturbed flow, the geometry of the stenotic lesion itself strongly influences local hemodynamics. Two factors are particularly important: the depth of stenosis, expressed as the percentage reduction in lumen diameter, and the shoulder length, defined as the axial distance over which narrowing occurs. Increasing stenosis depth is directly associated with higher velocity jets, larger pressure drops, and elevated WSS, all of which intensify endothelial dysfunction and thrombosis risk. For this reason, computational studies commonly examine stenosis severities of 30%, 50%, and 70%, corresponding to mild, moderate, and severe narrowing. The shoulder length modifies the steepness of the stenotic transition, which in turn alters flow separation and recirculation. Short shoulders generate sharper gradients that accelerate flow and amplify downstream vortices, whereas longer shoulders yield smoother transitions and less disturbed flow patterns Karimi et al. [18]. These differences are clinically relevant, as regions of post-stenotic recirculation characterised by low and oscillatory WSS are not only prone to plaque progression but also provide favourable conditions for nanoparticle adhesion and retention. Figure 2 illustrates this concept by showing arteries with varying stenosis depths, where progressive narrowing increases flow disturbance and alters downstream hemodynamics. Taken together, stenosis depth and shoulder length are fundamental determinants of the hemodynamic environment. Their inclusion in computational models enables systematic assessment of how lesion severity and geometry interact with blood rheology and pulsatility to shape both vascular pathology and nanoparticle delivery outcomes.

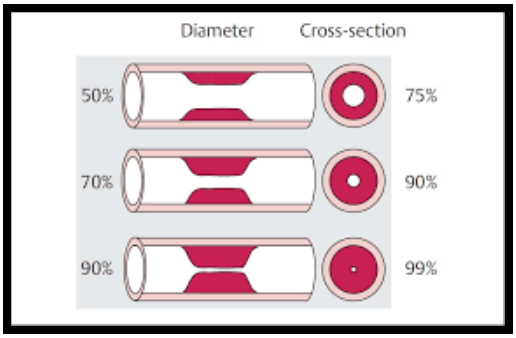

Fig 2: Arteries with varying stenosis depths illustrating progressive narrowing and altered flow patterns

The majority of previous computational studies of arterial blood flow have typically isolated either pulsatility or non-Newtonian characteristics when modelling hemodynamics. For example, Newtonian pulsatile models capture systolic flushing and diastolic particle deposition but neglect viscosity variation, while steady non-Newtonian models reproduce shear-dependent viscosity but overlook temporal oscillations in the blood flow. As a result, there is limited literature regarding which factor, pulsatility or non-Newtonian rheology, exerts a stronger influence on velocity distribution, wall shear stress (WSS) and nanoparticle deposition in stenosed arteries. Although some studies have completed direct comparisons of all four regimes (steady Newtonian, steady Carreau, pulsatile Newtonian, and pulsatile Carreau), it remains scarce in the context of stenotic blood flows and their treatment with for example, targeted nanoparticle drug delivery. Consequently, it is still unclear whether time-varying flow or shear-thinning viscosity has greater physiological significance near plaques, where disturbed hemodynamics govern both disease progression and therapeutic particle retention. To address this gap, the present study focuses on the two stenotic hemodynamic cases: 1] Steady Newtonian hemodynamics representing the baseline simplified assumption, and 2] pulsatile Carreau hemodynamics, representing the most physiologically realistic model. Simulations were performed across nine stenosed artery geometries (three stenosis severities each with three shoulder lengths) to capture a wide range of hemodynamic conditions. By quantifying pressure drop, velocity distribution and wall shear stress (WSS) for both cases 1] and 2], the present study systematically evaluates how pulsatile effects and hemo-rheology interact in stenotic flows. This targeted comparison clarifies the relative importance of these modelling choices and provides a rationale for selecting appropriate hemodynamic models in future nanoparticle-based therapeutic studies. Although we consider only 2-D simulations, a solid platform is established for future extensions

to 3-D flows and also fluid-structure interaction (FSI) with deformable arteries and a platform for extension to nanoparticle transport.

2. Modelling and blood flow physics

Hemodynamic transport in arteries can be explored using a range of modelling assumptions, broadly divided into steady versus pulsatile and Newtonian versus non-Newtonian approaches. Each combination provides unique insights while carrying distinct advantages and limitations for simulating disease-prone regions and evaluating drug (e.g. nanoparticle) delivery.

2.1. Steady Newtonian

Steady Newtonian flow assumes viscosity is constant and independent of shear rate, with flow properties such as velocity and WSS remaining constant over time. The governing relation is given by Bird, Stewart & Lightfoot [19]:

$$\tau = \mu\dot{\gamma} \tag{1}$$

Here τ is Shear Stress (N/m^2), μ is dynamic viscosity (kg m/s) and $\dot{\gamma}$ is shear rate (/s) This simplification is computationally efficient and often sufficient in large arteries, where high shear rates reduce non-Newtonian effects (White [20]) and Mandal [17]). However, it lacks accuracy in disturbed flow regions, where local hemodynamics drives both plaque development and for example nanoparticle adhesion in pharmacodynamic treatments.

2.2. Navier Stokes Equations

The Navier-Stokes equations for 3-D unsteady viscous laminar flow form the foundation of Newtonian flow simulation in blood flows assuming constant viscosity (μ), which does not vary with the shear rate. The full three-dimensional Navier–Stokes equations for unsteady viscous laminar flow are very challenging to solve, even with CFD software. In this article, we reduce them to the 2D equations by setting the out-of-plane velocity component and its derivatives to zero, which eliminates the z-momentum equation. The governing conservation equations in an (x,y) coordinate system for the *general 2-D unsteady hemodynamic case*, are:

Mass conservation:

$$\left[\frac{\partial u}{\partial x} + \frac{\partial v}{\partial y}\right] = 0 \tag{2}$$

The x-direction momentum conservation:

$$\rho\left[\frac{\partial u}{\partial t} + u\frac{\partial u}{\partial x} + v\frac{\partial u}{\partial y}\right] = \rho F_x - \frac{\partial p}{\partial x} + \mu\left[\frac{\partial^2 u}{\partial x^2} + \frac{\partial^2 u}{\partial y^2}\right] \tag{3}$$

The y-direction momentum conservation:

$$\rho\left[\frac{\partial v}{\partial t} + u\frac{\partial v}{\partial x} + v\frac{\partial v}{\partial y}\right] = \rho F_y - \frac{\partial p}{\partial y} + \mu\left[\frac{\partial^2 v}{\partial x^2} + \frac{\partial^2 v}{\partial y^2}\right] \tag{4}$$

Here (u, v) are the (x, y) direction *velocity components (m/s), P* is pressure (Pa), ρ is fluid density (*kg/m*^{3}), μ is dynamic viscosity (kg/ms), $\nu = \mu/\rho$ is kinematic viscosity (m^2/s), t is time (s), F_x, F_y are the body forces (which may be gravitational, body acceleration etc.) (*N*), $\frac{\partial p}{\partial x}$ is the x-direction pressure gradient (*Pa/m*) and $\partial p/\partial y$ is the y-direction pressure gradient (*Pa/m*). Blood can be modelled as Newtonian (for larger vessels) but is non-Newtonian in narrower vessels e.g. stenotic geometries, so the Navier-Stokes equations must be modified with a rheological model. e.g. Carreau shear-thinning, which is available in ANSYS FLUENT CFD software [21].

2.3. Steady Non-Newtonian (Carreau) model

The Carreau model incorporates shear-dependent viscosity, enabling a more realistic description of blood's shear-thinning behaviour. At low shear, blood behaves as a Newtonian fluid, while at high shear the behaviour approximates to that of a non-Newtonian power-law fluid (Khan et al. [22] and Nader et al. [16]). This approach is particularly useful in near-plaque, low-shear zones, where viscosity rises and WSS decreases, conditions strongly associated with platelet activation, thrombosis, and nanoparticle retention (Johnston et al. [10] and Soulis et al. [23]). The Carreau model is defined following Gendy et al. [24] as:

$$\mu = \mu_\infty + (\mu_0 - \mu_\infty)[1 + \lambda\gamma^2]^{\frac{n-1}{2}} \tag{5}$$

Here the μ is viscosity, $\mu_\infty = 0.00345\ Pa \cdot s$. is the infinite shear viscosity, $\mu_0 = 0.0560 Pa \cdot s$ is the blood viscosity at zero shear rate, λ =3.13s is the time constant, γ is the instantaneous shear rate and $n = 0.3568$ is the rheological power-law index. Selection of the Carreau model option in ANSYS FLUENT modifies the appropriate

terms in the basic Newtonian viscous model. Many successful applications of this model have been communicated in previous studies of blood flows for a range of applications- see Ali et al. [25], Mamun et al. [26] and Gambaruto et al. [27]. A key hemodynamic parameter is the wall shear stress (WSS) which is useful for predicting and estimating distributed flow conditions and the development of local atherosclerotic plaque. WSS is calculated using:

$$\tau_w = \mu \frac{\partial u}{\partial y} = \mu \cdot \dot{\gamma} \tag{6}$$

Here $\dot{\gamma}$ is deformation rate and $\partial u/\partial y$ is axial spatial velocity gradient.

2.4. Pulsatile Newtonian Case

Incorporating the cardiac cycle waveform into Newtonian simulations adds temporal variation while keeping viscosity constant. During systole, elevated flow velocities lead to high WSS, flushing nanoparticles downstream. In diastole, reduced velocities create low WSS, allowing drug nanoparticles to linger and adhere to the vessel wall, as noted by De Nisco et al. [28] and Sequeira et al. [29]. While this model captures cyclic flow dynamics, it may overpredict WSS magnitudes by neglecting non-Newtonian shear-thinning effects. In terms of the boundary conditions applied in this investigation, a medically precise pulsatile velocity profile was set at the inlet and is shown in Figure 3 and 80 mmHg of pressure was predicated for the outflow based on the study done by Carvalho et al. [30]. The inlet and outlet are fixed in all directions, and the vessel wall boundaries are established as a fluid-structure interface. The pulsative velocity profile is converted into a text file and inserted into the analysis as shown in figure 3. The CFD simulation is set as transient due to the heartbeat and pulsation effect.

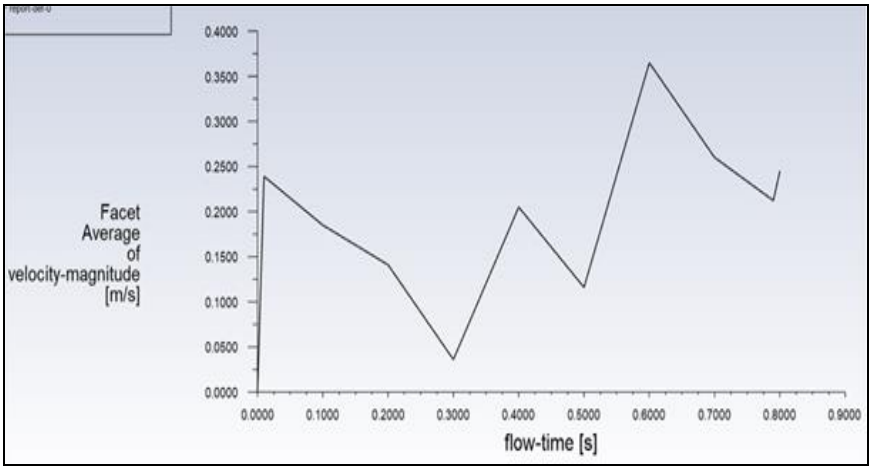

Fig 3: Pulsatile wave form deployed in ANSYS FLUENT simulations

2.5. Pulsatile non-Newtonian Case

The most physiologically realistic approach combines pulsatile effects with the Carreau model. Here, viscosity varies dynamically with shear rate: it decreases during systole, amplifying velocity peaks and WSS, but increases during diastole, particularly in recirculation zones, prolonging nanoparticle residence time in pharmacodynamics. This model best reproduces the complex hemodynamic of stenosed arteries, though it is computationally intensive.

3. Ansys Fluent CFD modelling

This study adopts a computational fluid dynamics CFD approach to investigate blood flow in a two-dimensional stenosed artery. The methodology is designed to capture the hemodynamic characteristics of blood under both steady and pulsatile flow conditions, incorporating its shear-thinning behaviour through a non-Newtonian viscosity model. We describe each stage below:

3.1. Geometry Creation

Three different shoulder length geometric cases are examined based on choice of shoulder lengths (2 mm, 4 mm, 6 mm) which correspond to short, intermediate and long scenarios respectively, and for each of these shoulder length cases three different stenosis depths (30%, 50%, 70%) are considered which correspond respectively to *mild, intermediate and severe*. Effectively 9 cases are therefore considered. These allow a systematic examination of geometric effects of the stenosis on velocity jet formation, wall shear stress distribution, and recirculation zones. The range of models is summarised in **Table 1** below:

Table 1. Stenosed artery models generated in SolidWorks for different the three different shoulder lengths (2 mm, 4 mm, 6 mm) and stenosis depths (30%-mild, 50%-intermediate, 70%-severe) considered for each case.

Geometric characteristics for different cases	**Case**		
	Short	Intermediate	Long
Shoulder length	2mm	4mm	6mm
Stenosis severity considered	30 %, 50%, 70%	30 %, 50%, 70%	30 %, 50%, 70%

Using SolidWorks, a corner rectangle is generated to represent the artery Domain, with a height of 6 mm and a width of 50 mm. To generate the stenosis, a shoulder length of 2 mm was then applied using the Smart Dimension tool. This dimension was later adjusted for each case to reflect the different shoulder lengths considered in the study. Splines were created on both the top and bottom edges of the rectangle, connecting symmetric points on the top and bottom edges on the domain, with their apex constrained to coincide with the vertical centreline. A stenosis depth was then applied, which varied according to the required severity (30%, 50%, or 70%). To ensure smooth continuity, the spline on the top edge was made tangent to the top boundary of the rectangle, while the spline on the bottom edge was constrained to the lower boundary. With the splines constrained to the top and bottom edges of the rectangle, the excess lines were trimmed, leaving the final profile of the stenosis. A planar surface was applied to the completed geometry, preparing the model for export into ANSYS, where the meshing process could be carried out. Fig. 4 shows the final geometry of the stenosed artery.

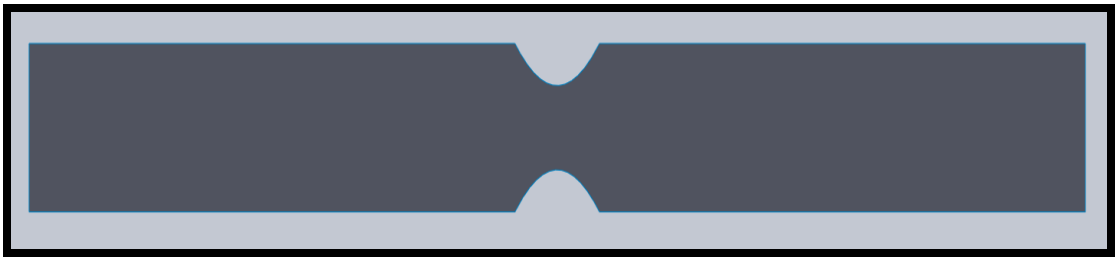

Fig 4: Completed stenotic arterial geometry.

3.2. Meshing

The meshing process plays a crucial role in influencing the numerical solution procedure for solving the governing equations over a defined domain. While the geometry step defines the domain, meshing determines how the mathematical model is numerically discretised for computation. Below is the detailed meshing methodology used. The computational mesh was generated in ANSYS Fluent with physics preference set to CFD and solver preference set to Fluent to ensure compatibility with fluid flow simulations. A uniform quadrilateral element size of 0.9 mm was initially used, with systematic refinements applied down to 0.5 mm to evaluate mesh independence. The Quad Dominant method was selected for surface meshing to achieve structured element distribution, while the Sweep method was employed for volume meshing in sweepable bodies. These settings provided a balance between mesh quality and computational efficiency, ensuring that flow gradients near the walls were adequately captured. The initial mesh design is shown in **Fig. 5**.

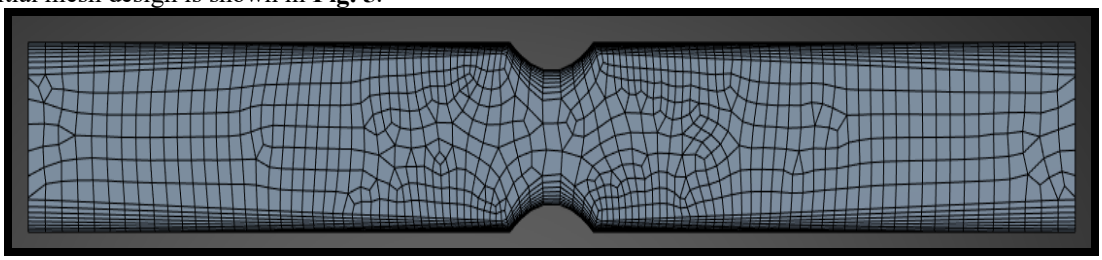

Fig 5: Mesh generated

Named selections were generated in Ansys Fluent in accordance with the regions shown in **Figure 6**. This process involved identifying the relevant edges within the geometry, assigning them as distinct entities, and labelling each with their appropriate descriptive name. This ensured that boundary conditions could be applied systematically and consistently during the simulation setup.

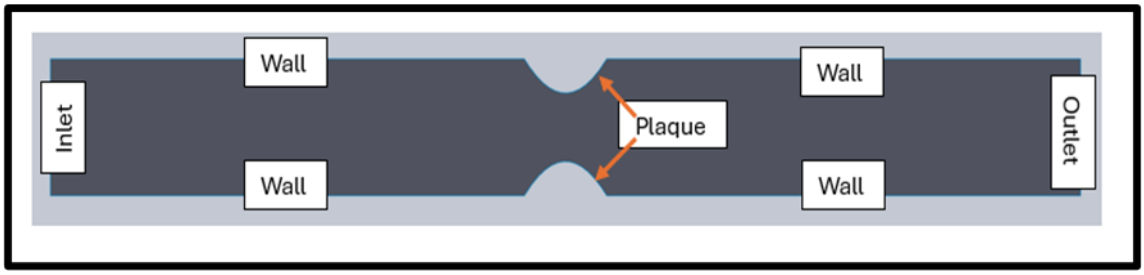

Fig 6: Named selection in stenotic arterial geometry

A quadrilateral dominant meshing strategy was employed for all stenosed artery models, as shown in Figure 11. This method generates quadrilateral elements, which provide improved accuracy and stability for capturing velocity gradients and wall shear stresses in 2D arterial flows. Where necessary, a limited number of triangular elements were permitted to ensure mesh conformity in complex geometrical regions, particularly around the stenosis shoulders. This approach ensured a balance between computational efficiency and numerical accuracy in resolving near-wall hemodynamics. An element size of 0.5 mm was applied. A bias factor of 3.0 was applied to refine elements toward the stenosis throat. This ensured that the mesh gradually decreased in size along the chosen edge, allowing finer resolution where steep velocity gradients and high wall shear stresses were expected, while coarser elements were maintained upstream to reduce computational cost. Curvature capture was enabled to accurately represent the curved arterial geometry, and smooth transitions between neighbouring elements were enforced to avoid abrupt changes in element size. This produced a progressively refined mesh concentrated around the stenosed region, which is critical for accurately capturing near-wall hemodynamics and nanoparticle deposition. A uniformly fine mesh across the entire artery was avoided, as this would have resulted in excessive computational cost without significantly improving accuracy in regions of relatively uniform flow. Instead, local refinement using edge sizing with a bias factor ensured that mesh density was concentrated in the stenosed region, where strong velocity gradients and wall shear stresses occur, while coarser elements were maintained elsewhere to optimise efficiency. To accurately resolve near-wall flow behaviour, inflation layers were applied along the arterial wall boundaries. Inflation generates a series of progressively smaller elements normal to the wall, allowing the mesh to capture steep velocity gradients and WSS with higher accuracy. A maximum of eight layers were applied with a growth rate of 1.2, providing a smooth transition from the boundary to the core flow region. A smooth transition option was selected to avoid abrupt element size changes, while the pre-inflation algorithm ensured that layers were inserted prior to the surface meshing step, maintaining good element quality. The inclusion of inflation layers is critical for hemodynamic simulations, as accurate representation of near-wall gradients directly affects the prediction of WSS, which is a key parameter in both plaque progression and nanoparticle deposition. The mesh was generated for each geometry (30%, 50% and 70% stenosed at 2mm, 4mm and 6mm shoulder lengths). **Figure 7** below displays an example of the finalised mesh for the 30% stenosed artery with a 2mm shoulder length.

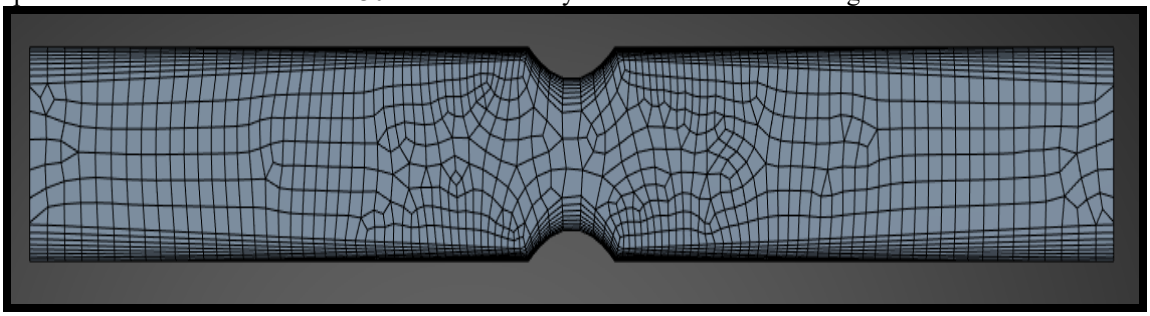

Fig 7: Final Mesh

3.3. Mesh Refinement Study

Mesh independence is a critical step in CFD studies to ensure excess computational power is not used to generate a result of a simulation which could be run at a larger element size i.e. with lower mesh density. In this work, a systematic mesh refinement study was conducted to determine the appropriate element size for accurate and computationally efficient simulations of blood flow in stenosed arteries. Five levels of mesh resolution were tested, with element sizes ranging from 1.0 mm (coarse) to 0.5 mm (extra fine). Intermediate refinements were performed at 0.9 mm, 0.8 mm, 0.7 mm, and 0.6 mm. Each mesh was generated using the quadrilateral-dominant method with edge sizing applied near the stenosis throat to resolve regions of high velocity gradients and steep WSS. Inflation layers were maintained consistently across all meshes to capture near-wall effects. **Table 2** below outlines the mesh

sizes used across the body of the artery and on the plaque and walls. The mesh independence study was conducted using six progressively refined meshes with densities ranging from 2123 cells (coarse, Case F)) to a maximum of 4461 cells (extra fine, Case A). The medium mesh density with 2717 cells (case D) was selected for subsequent simulations as higher mesh densities produced negligible changes in the results while increasing computational cost. All details are summarized in **Table 2**.

sizes, mesh refinement cases and total cell count (mesh densities)

Mesh Design Case	Element Size Description	Total Number of Cells (Mesh Density)
A	0.5mm element size-Extra fine	4461
B	0.6mm element size- Extra fine	3645
C	0.7mm element size-Fine	3106
D	0.8mm element size- Medium	2717
E	0.9mm element size-Medium	2335
F	1.0mm element size- Coarse	2123

We have further summarized the mesh independence design study in **Table 3** identifying the final design implemented for all simulations i.e. Case D.

Table 3. Summary of element sizes, total cell counts (mesh densities) and the design selected for utilizing in simulations

Mesh Density Level	Element Size	Total Number of Cells	Deployed in Final Simulations
COARSE (Case F)	1.0 mm element size	2123	No
MEDIUM (Case D)	0.8mm element size	2717	Yes
FINE (Case A)	0.5mm element size	4461	No

To ensure a consistent ratio was maintained between the global body mesh and the local edge sizing near the plaque, a refinement ratio was used.

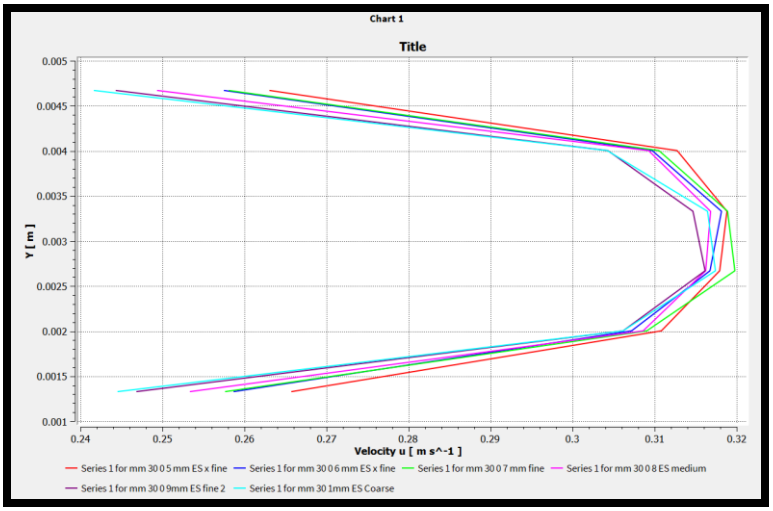

Fig 8: Convergence test with different mesh densities for velocity profiles at the centreline downstream of a 30% stenosis with a 2 mm shoulder length

Figure 8 presents the velocity profiles at the centreline downstream of a 30% stenosis with a 2 mm shoulder length, comparing results across the different mesh densities, as part of the convergence test. The coarse mesh (1.0 mm element size) shows noticeable deviation from the finer meshes, particularly in the velocity peak and boundary layer resolution. As the mesh is refined to 0.9 mm and 0.8 mm, the velocity distribution begins to converge, but slight discrepancies remain near the stenosis throat. At 0.7 mm and 0.6 mm, the profiles are nearly identical to the finest 0.5 mm mesh, indicating that mesh independence has been achieved. The results demonstrate that below an element size of approximately 0.7 mm, further refinement produces negligible change in the velocity profile. While the 0.5 mm mesh provides the most detailed resolution, it also significantly increases computational cost. To balance accuracy with efficiency, a *hybrid meshing strategy* was adopted in which a global element size of 0.9 mm was applied to the bulk domain, while a finer edge sizing of 0.5 mm was enforced near the stenosis and arterial walls. This ensured that mesh density was concentrated in regions of steep velocity gradients and high WSS, while the remainder of the flow, characterised by smoother gradients, was resolved adequately with larger elements. The 0.9 to 0.5 mm transition provides a refinement ratio of approximately 1.8, and, when combined with the inflation layers and biasing toward the throat, achieves the same level of accuracy as the uniformly fine meshes of less than or equal to 0.7mm but at a fraction of the computational cost. This mesh refinement study therefore confirms that the chosen

configuration is both reliable and efficient, providing confidence that subsequent results reflect the underlying physics of blood flow.

3.4. Setup - Steady Newtonian Simulation

During the setup stage in ANSYS Fluent, the imported mesh is prepared for simulation by defining the governing physical models and boundary conditions. This includes specifying the material properties, selecting the flow model, and enabling turbulence or laminar flow as appropriate. Boundary conditions such as inlet velocity profiles, outlet pressure, and no-slip arterial wall constraints are then applied to the named selections generated during meshing. Together, these steps establish the physical and numerical framework that ANSYS Fluent uses to solve the governing equations of fluid flow. The solver was configured for the steady Newtonian simulations and later configured for Pulsatile Non-Newtonian (Carreau). The pressure-based solver was selected, appropriate for incompressible flows. The simulation was defined as steady-state, assuming flow properties remained time-invariant throughout the computational domain. A 2D planar configuration was chosen to represent the artery cross-section, reducing computational cost while capturing the essential flow behaviour. The velocity formulation was set to absolute, and gravitational effects were disabled, as they are negligible for horizontal arterial flow in this simplified model. The laminar viscous model was selected which solves the full Navier-Stokes equations without additional turbulence modelling, which is appropriate given that arterial blood flow in this study occurs at laminar Reynolds numbers.

3.4.1 Material Properties

The fluid was defined as "blood", with its properties specified under the Newtonian assumption. A constant density of 1060 kg/m^3 and a constant viscosity of 0.0035 (kg/m/s) were applied, values consistent with those commonly used in hemodynamic simulations of large arteries. These constants reflect the high shear rate limit of blood behaviour, where non-Newtonian effects become negligible and viscosity approaches a near-constant value, as noted in Ballyk et al. [11]. The fluid domain was assigned under the Cell Zone Conditions panel. Here, the material was specified as blood, ensuring that the defined density and viscosity values were consistently applied throughout the computational domain. No additional options such as frame motion, mesh motion, or porous zone were enabled, as the artery was modelled as a stationary 2D channel with a single-phase incompressible fluid. This step ensured that the simulation environment correctly reflected physiological flow conditions within the artery.

3.4.2 Boundary conditions

Boundary conditions are essential in CFD simulations as they define how the fluid interacts with the computational domain and ensure that the governing equations are solved under physically realistic constraints. For arterial blood flow, appropriate inlet, outlet, and wall conditions must be prescribed to replicate physiological conditions and to accurately capture flow behaviour and wall shear stresses. At the *inlet boundary*, a constant velocity of $0.2\ m/s$ was applied using the magnitude and direction method. Flow was aligned with the positive x-direction, while the y-component was set to zero, ensuring uniform horizontal entry into the domain. The reference frame was defined as absolute, consistent with a stationary artery model. This inlet velocity is within the physiological range of arterial blood flow and provides a steady inflow condition for the Newtonian simulations. At the *outlet boundary*, a pressure outlet condition was applied with a gauge pressure of 0 *Pa*, corresponding to atmospheric reference pressure. The backflow specification was set to total pressure, with flow direction normal to the boundary. This configuration allows fluid to exit the computational domain without artificial constraints while maintaining numerical stability in cases of minor flow reversal. Such an outlet condition is widely used in arterial CFD modelling, as it provides a physiologically reasonable representation of downstream flow resistance. The arterial walls and plaque surfaces were modelled as stationary, no-slip boundaries. Under this condition, the velocity of blood at the wall surface was set to zero, ensuring accurate capture of near-wall velocity gradients and WSS. Both surfaces were treated as "hydraulically smooth", with wall roughness specified as zero. This setup reflects physiological conditions in idealised arterial models, where wall motion is negligible and plaque surfaces are simplified as smooth boundaries.

3.4.3 Solution Setup, Initialization and Run

This section outlines the process of solving the governing equations, including configuring solution methods, setting residual tolerances, and initialising values. The governing equations of fluid flow were solved in ANSYS Fluent using the finite volume method (FVM), in which the computational domain is subdivided into control volumes and the conservation equations are applied in discretised form. To ensure accurate representation of convective transport, the second-order upwind scheme was used for momentum equations, which reduces numerical diffusion and provides more reliable predictions of velocity and wall shear stress compared to first-order schemes. Pressure interpolation was also performed using a second-order scheme to enhance spatial accuracy. The pressure–velocity coupling was resolved using the Semi-Implicit Method for Pressure Linked Equations (SIMPLE) algorithm, the standard iterative procedure for steady, incompressible flows in ANSYS Fluent. In this approach, provisional

velocity fields are obtained by solving the momentum equations, and a pressure correction equation derived from continuity is used to enforce mass conservation. The corrected velocity and pressure fields are then updated iteratively until convergence is achieved - see Kuharat et al. [31]. Numerical convergence was monitored through residuals. This ensured that the velocity field developed consistently downstream and that the pressure gradient correctly drove the flow from inlet to outlet. The use of second-order schemes in combination with the SIMPLE algorithm provided a robust and computationally efficient framework for accurately resolving arterial hemodynamics under the steady Newtonian assumption. The SIMPLE algorithm main advantages over transient solvers in ANSYS Fluent are faster convergence for steady-state flows**,** lower computational cost per iteration**,** and the ability to handle larger time steps in pseudo-transient or steady applications**,** making it efficient for stable flows where time evolution is not critical. SIMPLE achieves this through aggressive under-relaxation, allowing quicker progression towards a stable solution, whereas transient solvers (like PISO) focus on precise time-stepping, requiring more steps and potentially smaller time steps for accuracy, thus increasing computational expense. The solution was initialised in ANSYS Fluent using the hybrid initialisation method. Initialisation provides the solver with starting values of flow variables, such as velocity, pressure etc across the computational domain before the iterative solution process begins. Without this step, the solver would have no reference state from which to start convergence. The hybrid initialisation approach combines aspects of both standard and physical-based methods: it solves a simplified Laplace-like equation to generate a velocity and pressure field that is consistent with the boundary conditions and domain geometry. This results in faster and more stable convergence compared to standard initialisation, particularly in cases with complex flow patterns such as those found in stenosed arteries. Standard initialisation was not selected, as it generates uniform starting values that can lead to slower convergence or divergence in regions with strong velocity gradients. The simulation was executed through selecting Run Calculations. A maximum of 2000 iterations was specified to provide sufficient allowance for convergence, although in most cases residuals reached the target tolerance before this limit. The reporting interval was set to 1, ensuring that residuals and solution updates were displayed at every iteration for close monitoring of convergence behaviour. Similarly, the profile update interval was set to 1, allowing boundary profiles to be consistently updated each iteration.

3.5. Pulsatile Non-Newtonian (Carreau) Simulation

This section describes the configuration of the pulsatile non-Newtonian (Carreau) simulations, where blood viscosity is defined as shear-rate dependent and flow is driven by a time-varying velocity waveform. Compared to the steady Newtonian model, this setup introduces transient flow conditions and a more physiologically realistic viscosity distribution. The pressure-based solver was again selected, appropriate for incompressible flows. However, unlike the steady Newtonian case, the simulation was defined as transient to capture the time-varying pulsatile flow. As before, a 2D planar configuration was used and gravitational effects were neglected. The flow was still modelled as laminar, consistent with physiological Reynolds numbers. No turbulence model was applied, as pulsatile effects and viscosity variation dominate the flow behaviour in this regime.

3.5.1 Material Properties

Unlike the Newtonian case, blood was defined as a *non-Newtonian Carreau fluid*. The Carreau model was used to represent shear-thinning behaviour, with viscosity expressed as a function of shear rate. The rheological parameters were taken from Cho & Kensey [15] as displayed in **Figure 9**. These values allow viscosity to transition smoothly from Newtonian behaviour at low shear to power-law behaviour at high shear. This ensured that near-plaque, low-shear zones exhibited elevated effective viscosity, while systolic peaks were captured with reduced viscosity. Blood density is still 1060kg/m^3 as with the Newtonian case.

3.5.2 Boundary Conditions

The Inlet conditions were adjusted to satisfy those required for the Carreau Model. Instead of a constant velocity, a pulsatile velocity profile was applied based on the waveform given in **Fig. 3**, representing one cardiac cycle. The waveform was applied using a User-Defined Function (UDF). This allowed systolic acceleration and diastolic deceleration phases to be resolved. The same pressure outlet (0 *Pa*) for gauge pressure was applied as in the steady Newtonian case, enabling free outflow with total pressure backflow handling. No-slip boundary conditions were again applied to both walls and plaque surfaces, with zero roughness.

3.5.3 Solution Setup, Initialization and Run

The finite volume method (FVM) was again used with second-order upwind discretisation for spatial accuracy. However, due to the transient definition, a second-order implicit time discretisation scheme was also applied, ensuring accuracy in capturing pulsatile oscillations. Pressure-velocity coupling was again handled by the SIMPLE algorithm. Hybrid initialisation was applied to generate the starting field. The simulation was advanced in time using a fixed time-step approach. Initially a total of 600-time steps were specified, with a time-step size of 0.0025 s, corresponding to one full cardiac cycle. Each time step was allowed up to 20 iterations to ensure convergence within

the step. A reporting interval of 1 was set, meaning results were written and residuals monitored at every time step. The profile update interval was also set to 1, ensuring boundary conditions were updated consistently throughout the cycle. By advancing the solution in this way, transient oscillations in velocity and wall shear stress were fully resolved across the pulsatile waveform. After further time step sensitivity analysis, the final transient simulation used a fixed time step of 0.001 s over a total simulated time of 1 s, corresponding to one cardiac cycle, resulting in 1000 timesteps. A fixed time step was selected to maintain numerical stability and temporal accuracy, with convergence achieved at each time step within 20 inner iterations and Courant numbers maintained below unity.

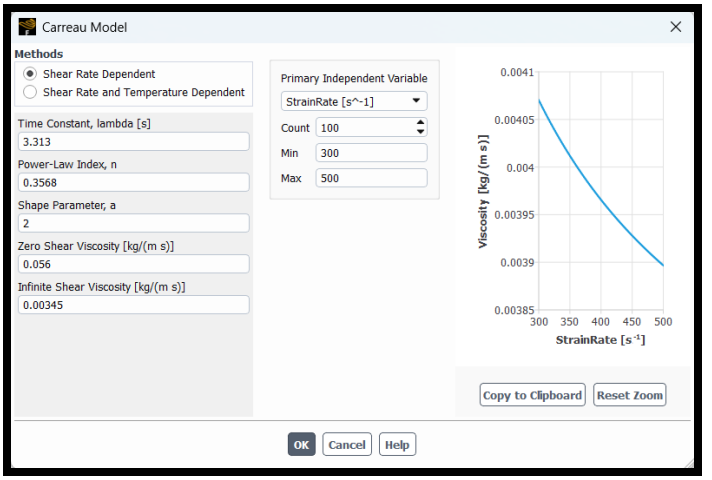

Fig 9: Carreau Model Properties

3.6 Comparison of Simulation Setup: Steady Newtonian vs Pulsatile Carreau

This dual-modelling approach strengthens the study by providing both a baseline reference and a physiologically realistic case. The steady Newtonian model offers computational efficiency and serves as a simplified benchmark, while the pulsatile Carreau model incorporates both time-dependent flow dynamics and shear-thinning viscosity, enabling more accurate prediction of velocity fields, wall shear stress, and nanoparticle behaviour. Together, these complementary models allow systematic assessment of how pulsatile effects and non-Newtonian rheology influence hemodynamic outcomes in stenosed arteries.

Table 4. Summary of comparison between the Steady Newtonian and Pulsatile Non-Newtonian cases simulated

Category	Steady Newtonian	Pulsatile non-Newtonian
Solver Type	Pressure based, Steady	Pressure based, Transient
Dimensionality	2D Planar	2D Planar
Viscosity Model	Constant Viscosity	Carreau non-Newtonian Model parameters
Density	1060 kg/m^3	1060 kg/m^3
Inlet Condition	Uniform velocity, 0.2 m/s	Pulsatile Velocity Waveform using UDF
Outlet Conditions	Pressure outlet, 0 Pa	Pressure outlet, 0 Pa
Walls and Plaque	Stationary, no-slip, smooth surface	Stationary, no-slip, smooth surface
Time	N/A	Fixed Time-step
Purpose	Baseline- Simple, computationally efficient	Physiologically realistic capturing shear thinning and cardiac pulsatility.

Table 4 presents the results side by side which not only highlights the differences in flow behaviour between steady Newtonian and pulsatile Carreau simulations but also clarifies the relative importance of pulsate effects and shear-thinning rheology in arterial drug delivery applications. By contrasting these two simulation setups, the subsequent results section can directly compare the hemodynamic predictions under simplified and physiologically realistic assumptions. This enables evaluation of how model choice influences key outcomes such as pressure drop, velocity distribution, WSS, and potentially also consider the implications of the hemodynamic characteristics on for example, nanoparticle residence in nano-drug delivery.

4. ANSYS FLUENT RESULTS AND DISCUSSION

4.1 Steady Newtonian Case- Velocity Plots

The steady Newtonian simulations provide a fundamental baseline for analysing blood flow behaviour within stenosed arteries. By assuming constant viscosity, these plots simplify the rheology of blood while still capturing the key hemodynamic features associated with arterial narrowing, including flow acceleration at the stenosis throat, the development of high-velocity jets, and the formation of recirculation zones downstream. Establishing this baseline is essential, as it validates the computational setup and highlights the primary flow structures before introducing additional physiological complexities such as *pulsatility and non-Newtonian shear-thinning effects*. Moreover, the steady Newtonian velocity plots serve as a reference point against which subsequent models can be compared, allowing the influence of pulsatility and rheology on velocity distribution, WSS, and nanoparticle deposition. Across all stenosis severities and shoulder lengths, the velocity increases sharply at the throat of the stenosis, with the highest velocity magnitudes consistently located at the narrowest cross-section. For 30% stenosis (Figures 10, 13, 16), flow acceleration is present but moderate, and the velocity distribution downstream quickly stabilises. At 50% stenosis (Figures 11, 14, 17), the peak velocity increases further, with a more pronounced jet extending downstream, accompanied by small regions of low velocity near the walls. At 70% stenosis (Figures 12, 15, 18), the velocity profile shows the greatest acceleration at the throat, with a distinct high-speed jet and extensive recirculation zones downstream. Increasing the shoulder length (from 2 mm to 6 mm) produces a smoother acceleration and deceleration of flow, with the longer shoulders displaying a more gradual transition of velocity compared to the abrupt changes observed for the shorter shoulders.

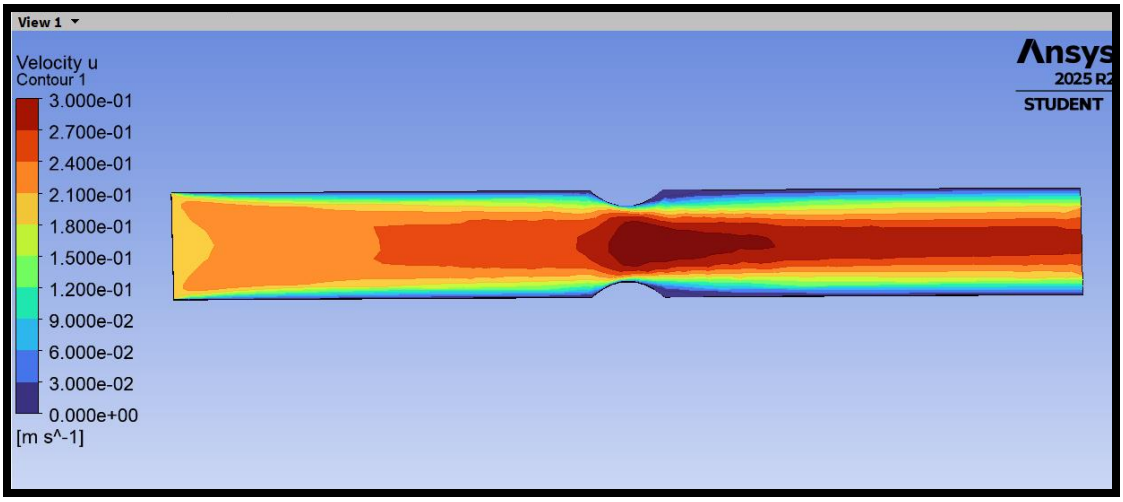

Fig 10: Velocity Profile for 2mm Shoulder Length with 30% Stenosis- Steady Newtonian

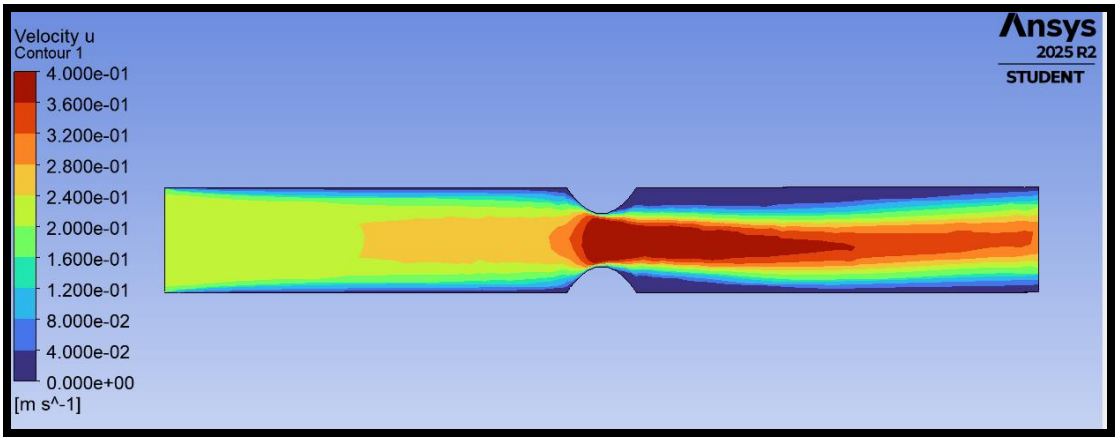

Fig 11: Velocity Profile for 2mm Shoulder Length with 50% Stenosis- Steady Newtonian

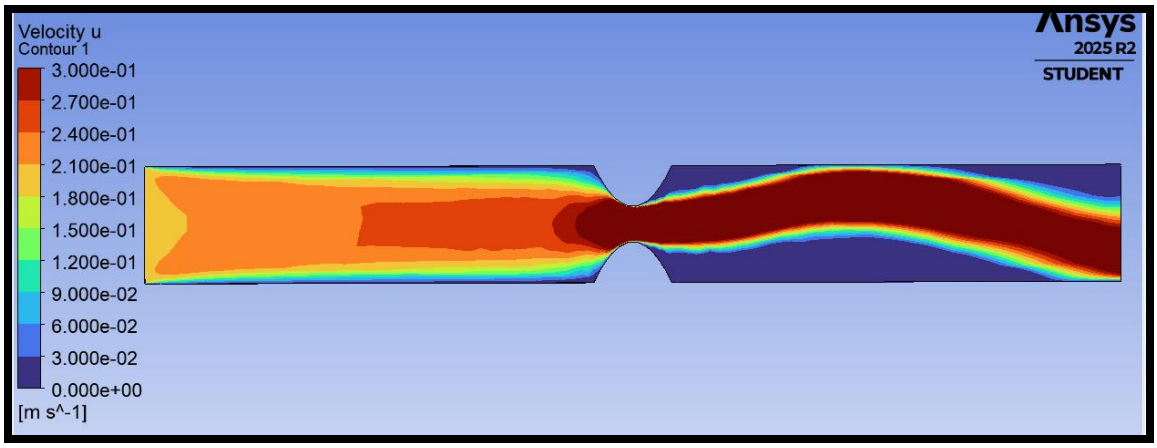

Fig 12: Velocity Profile for 2mm Shoulder Length with 70% Stenosis- Steady Newtonian

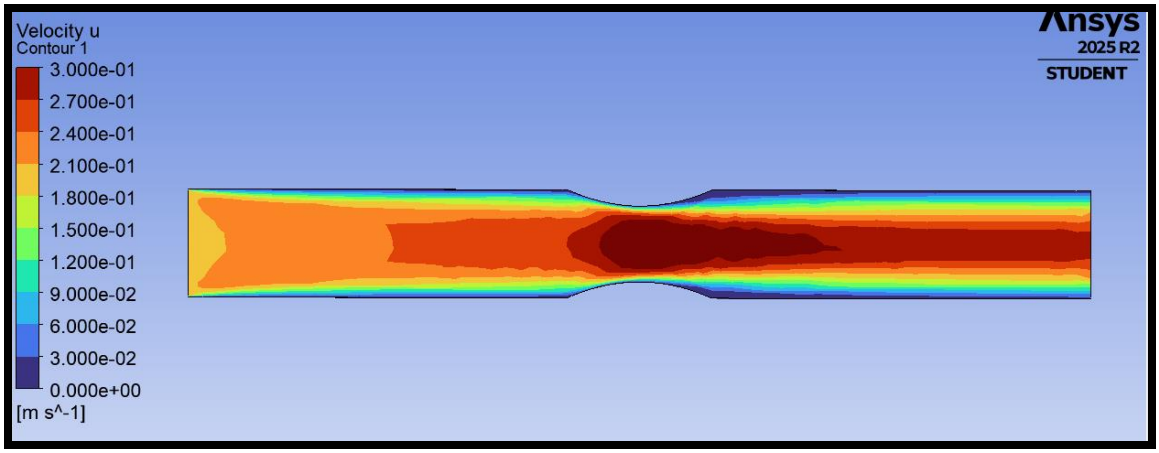

Fig 13: Velocity Profile for 4mm Shoulder Length with 30% Stenosis- Steady Newtonian

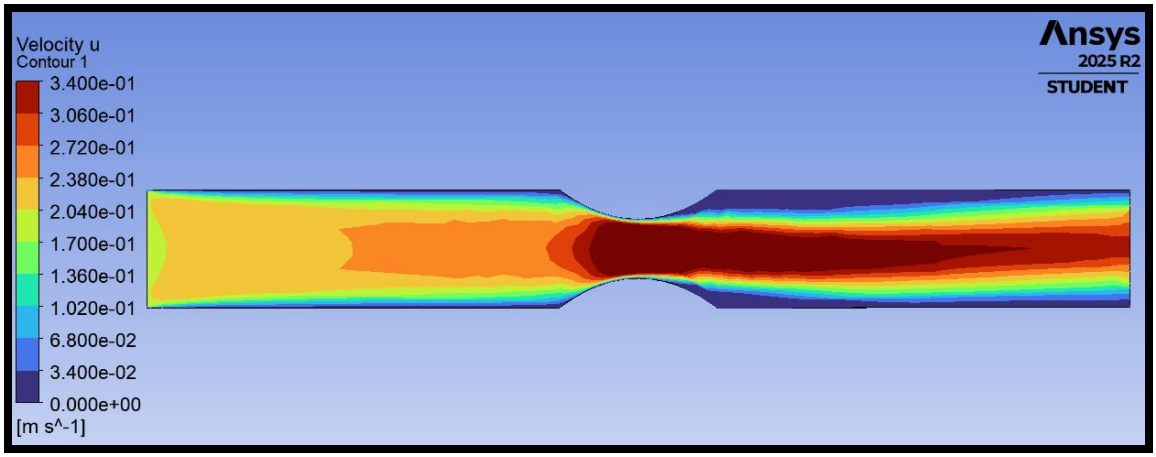

Fig 14: Velocity Profile for 4mm Shoulder Length with 50% Stenosis- Steady Newtonian

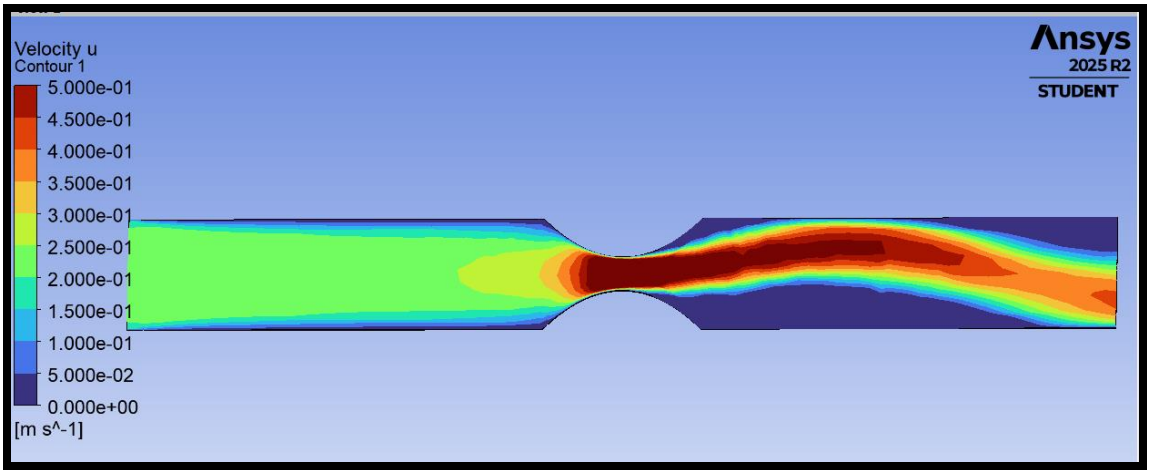

Fig 15: Velocity Profile for 4mm Shoulder Length with 70% Stenosis- Steady Newtonian

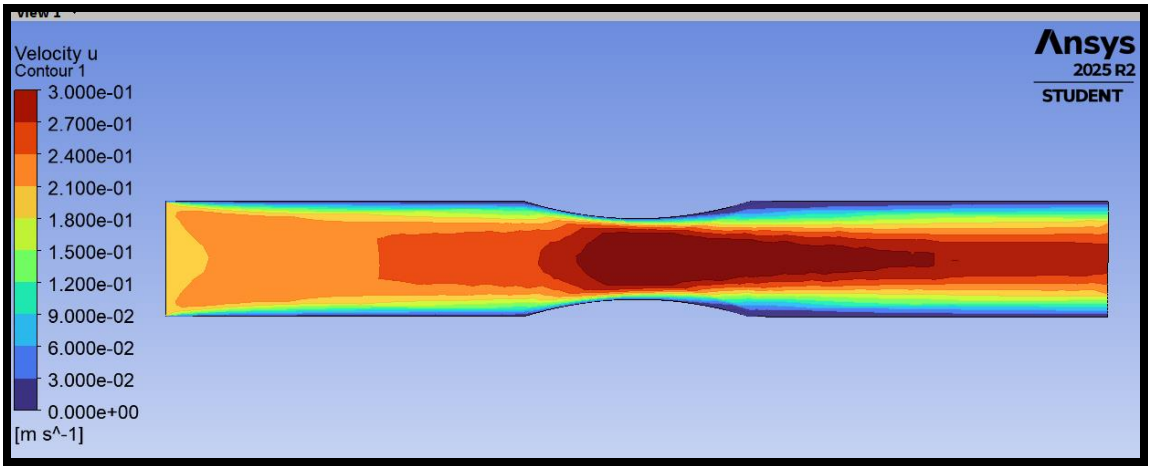

Fig 16: Velocity Profile for 6mm Shoulder Length with 30% Stenosis- Steady Newtonian

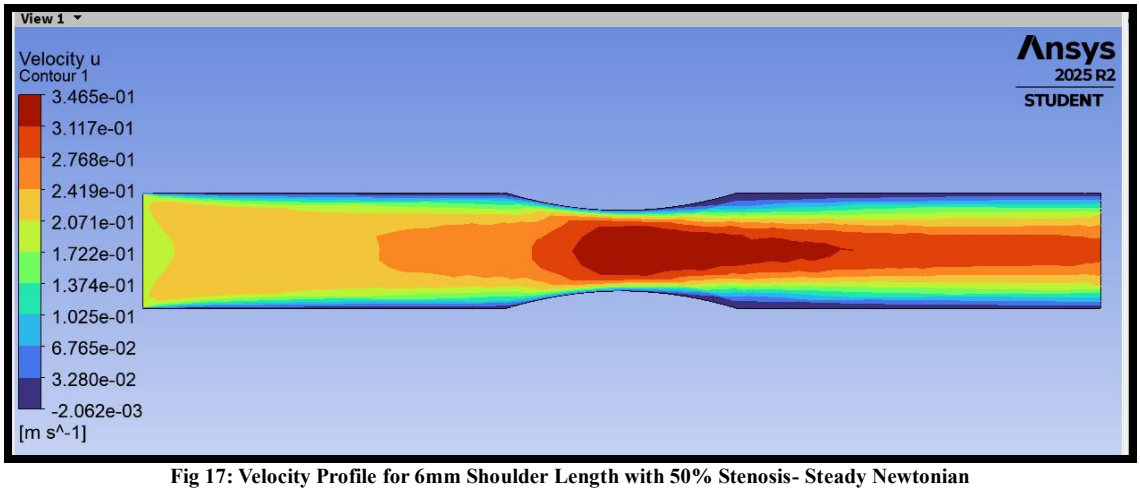

Fig 17: Velocity Profile for 6mm Shoulder Length with 50% Stenosis- Steady Newtonian

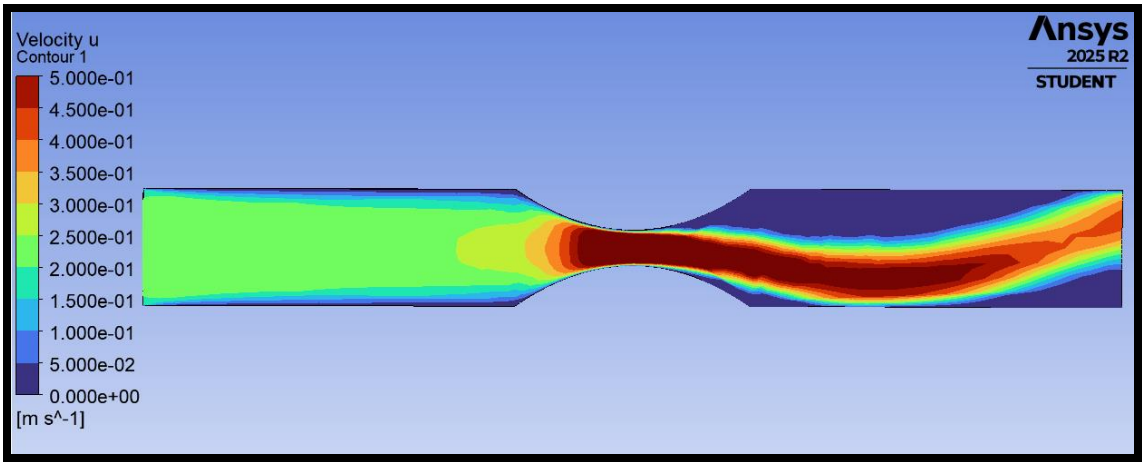

Fig 18: Velocity Profile for 6mm Shoulder Length with 70% Stenosis- Steady Newtonian

4.2 Pulsatile Non-Newtonian (Carreau) Case

4.2.1 Velocity Plots

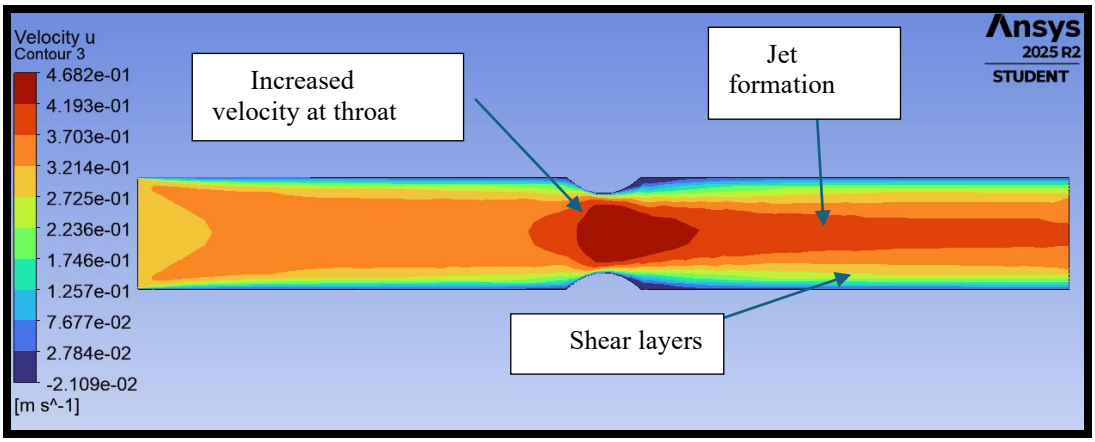

Fig 19: Velocity Profile for 2mm Shoulder Length with 30% Stenosis- Carreau

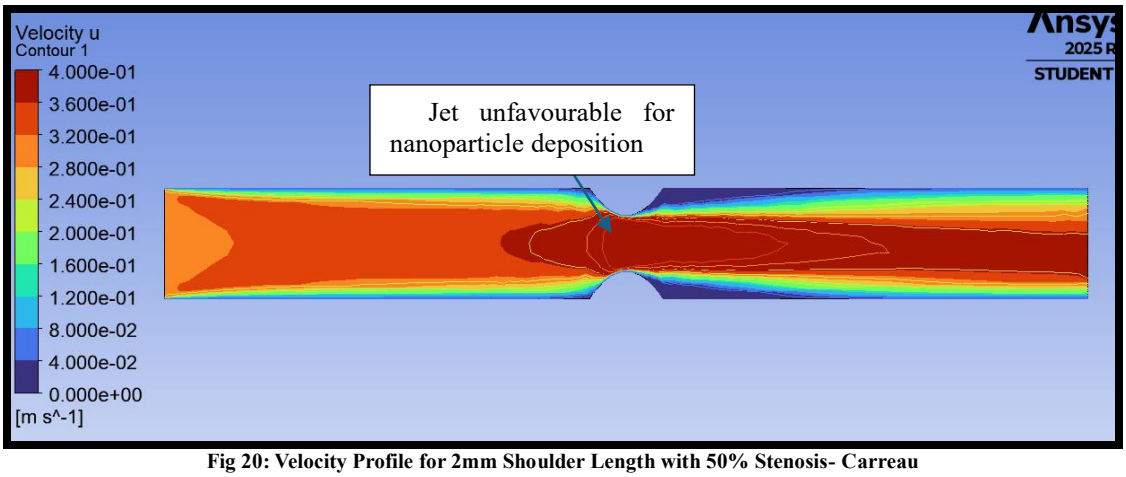

Fig 20: Velocity Profile for 2mm Shoulder Length with 50% Stenosis- Carreau

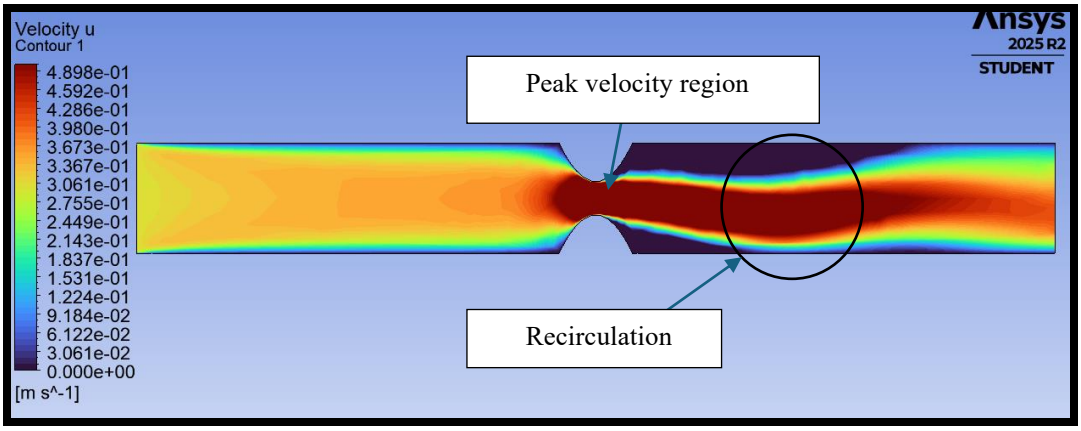

Fig 21: Velocity Profile for 2mm Shoulder Length with 70% Stenosis- Carreau

At 30% stenosis, the flow accelerates through the narrowed throat, creating a moderate velocity jet with a peak around 0.47 m/s (**Figure 19**). Disturbance is limited, with only small downstream recirculation zones that quickly reattach, indicating relatively stable flow. At 50% stenosis, the narrowing produces a stronger jet that extends further downstream, accompanied by larger recirculation zones near the vessel walls (**Figure 20**). This leads to more disturbed flow patterns and increased regions of low shear stress compared to the 30% case. In the 70% stenosis condition, the severe narrowing generates a highly accelerated jet at the throat, with peak velocities approaching 0.49 m/s (**Figure 21**). This strong jet induces large downstream recirculation zones and disturbed flow, creating conditions favourable for low-shear regions where nanoparticles may deposit.

The longer 4 mm shoulder creates a smoother acceleration of flow through the 30% stenosis, with peak velocities around 0.47 m/s distributed more gradually across the throat (**Figure 22**). Downstream flow remains relatively stable with minimal recirculation, indicating reduced flow disturbance compared to shorter shoulder lengths. At 50% narrowing, a strong velocity jet develops at the stenosis throat, reaching peaks above 0.65 m/s (**Figure 23**). Minimum magnitude was computed as approximately 0.0042m/s. The 4 mm shoulder produces a moderately extended transition, with downstream flow separation and recirculation clearly visible, highlighting disturbed haemodynamics that would potentially favour nanoparticle trapping. Under the severe 70% stenosis condition, an intense velocity jet exceeding 0.9 m/s forms at the throat (**Figure 24**). The 4 mm shoulder elongates the disturbed region, creating extended recirculation zones downstream that are likely locations for nanoparticle deposition.

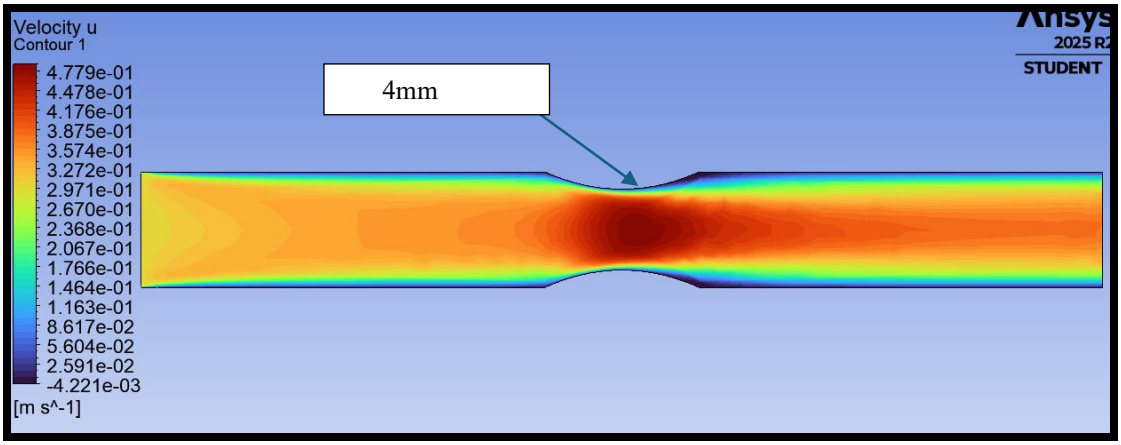

Fig 22: Velocity Profile for 4mm Shoulder Length with 30% Stenosis- Carreau

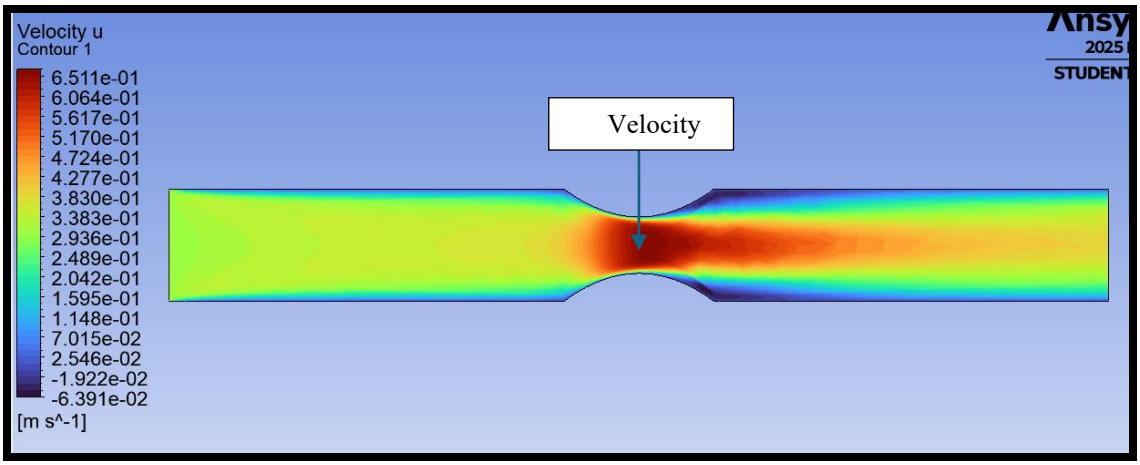

Fig 23: Velocity Profile for 4mm Shoulder Length with 50% Stenosis-Carreau

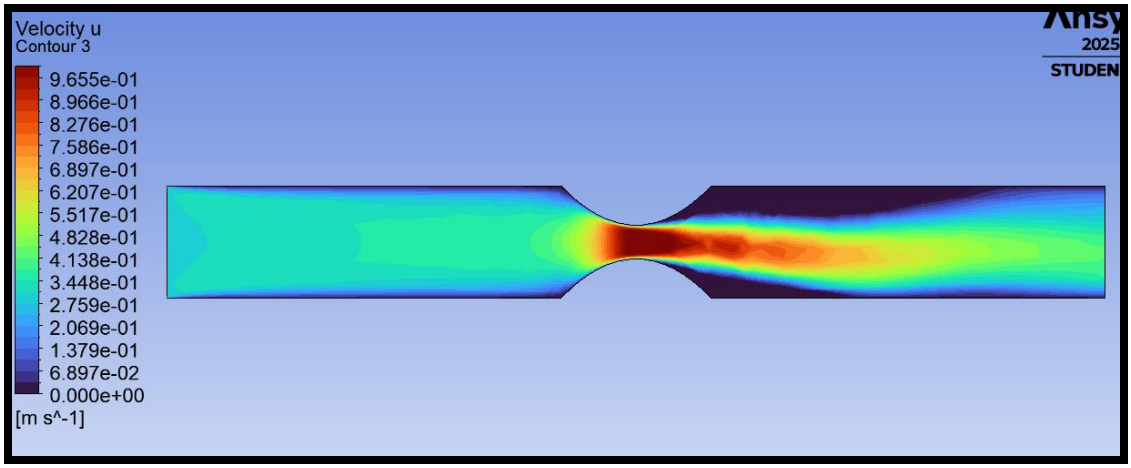

Fig 24: Velocity Profile for 4mm Shoulder Length with 70% Stenosis- Carreau

The 30% stenosis with a long 6 mm shoulder generates a mild acceleration of flow, with velocity smoothly increasing through the narrowing (**Figure 25**). Disturbance downstream is minimal, and the extended shoulder produces a gradual transition that reduces recirculation compared to shorter shoulders. At 50% stenosis (**Figure 26**), a strong velocity jet forms at the throat, with smoother acceleration than observed in shorter-shouldered cases. Although the extended shoulder reduces the sharpness of flow separation, a broad disturbed region still develops downstream, creating conditions that may enhance nanoparticle residence in low-shear zones. In the most severe case of 70% stenosis, an intense and narrow jet is produced at the throat, with peak velocities approaching 0.68 m/s approximately (**Figure 27**). Minimum values were computed as 0.048m/s. The longer shoulder smooths the inflow but extends the downstream disturbed flow and recirculation region, resulting in a broad low-velocity zone that is highly favourable for nanoparticle deposition.

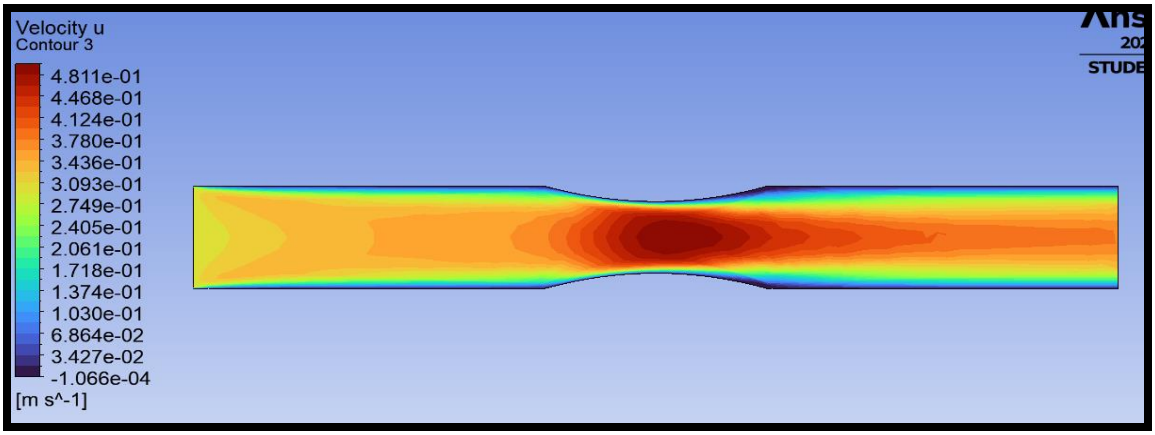

Fig. 25: Velocity Profile for 6mm Shoulder Length with 30% Stenosis- Carreau

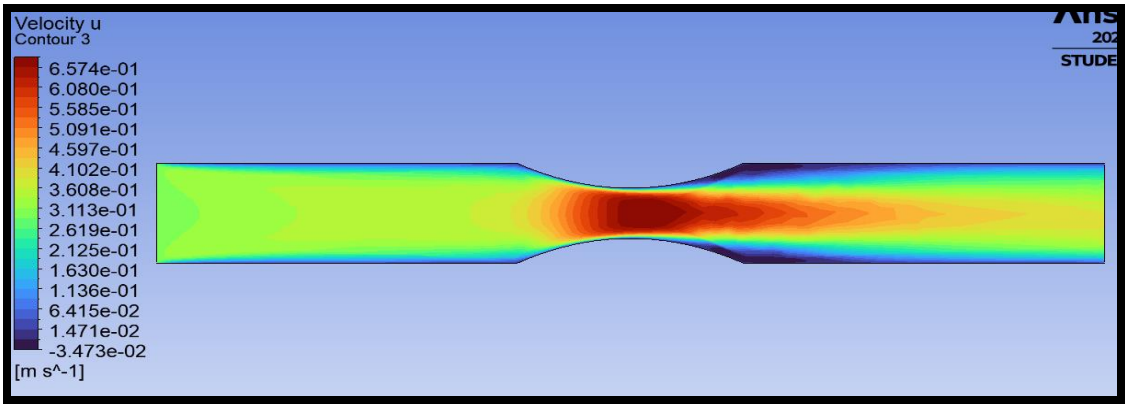

Fig 26: Velocity Profile for 6mm Shoulder Length with 50% Stenosis- Carreau

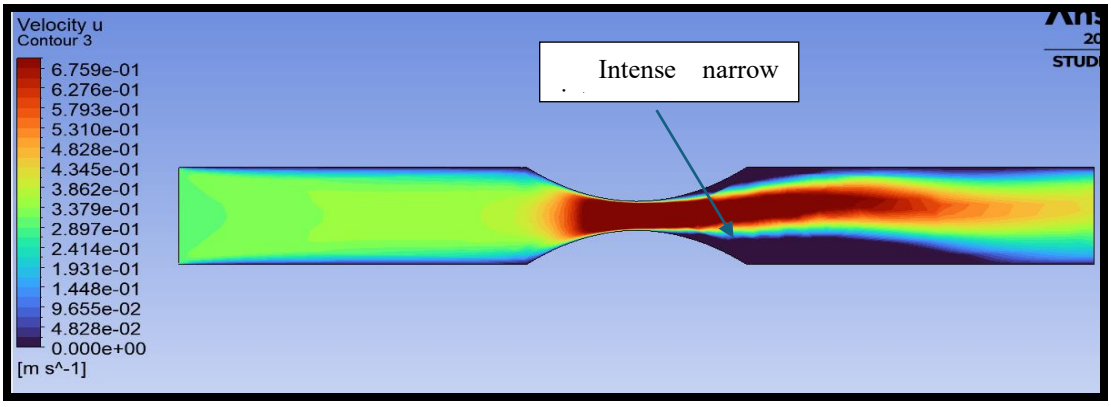

Fig 27: Velocity Profile for 6mm Shoulder Length with 70% Stenosis- Carreau

Additionally for this non-Newtonian pulsatile case, we have displayed pressure plots, described in the next sub-section.

4.2.2 Pressure distribution contour plots

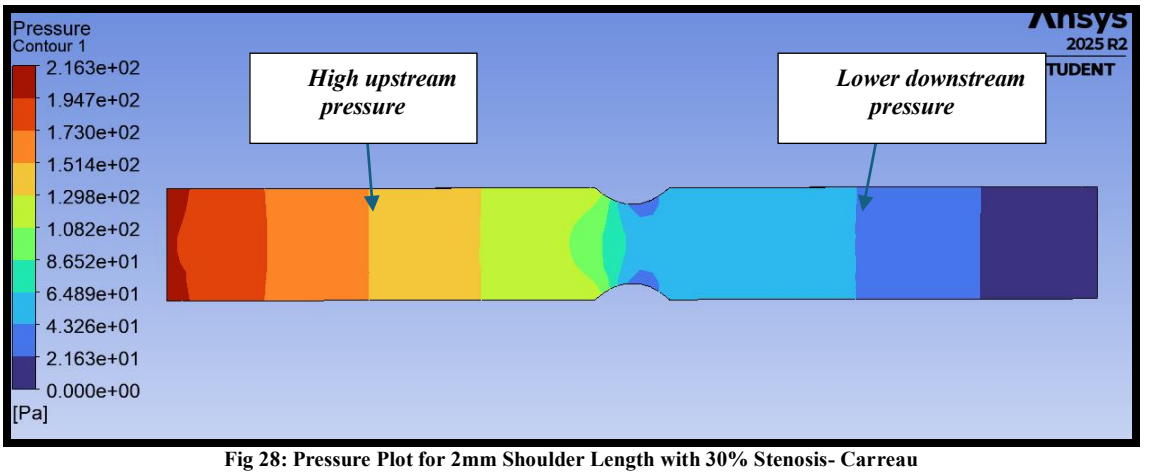

Fig 28: Pressure Plot for 2mm Shoulder Length with 30% Stenosis- Carreau

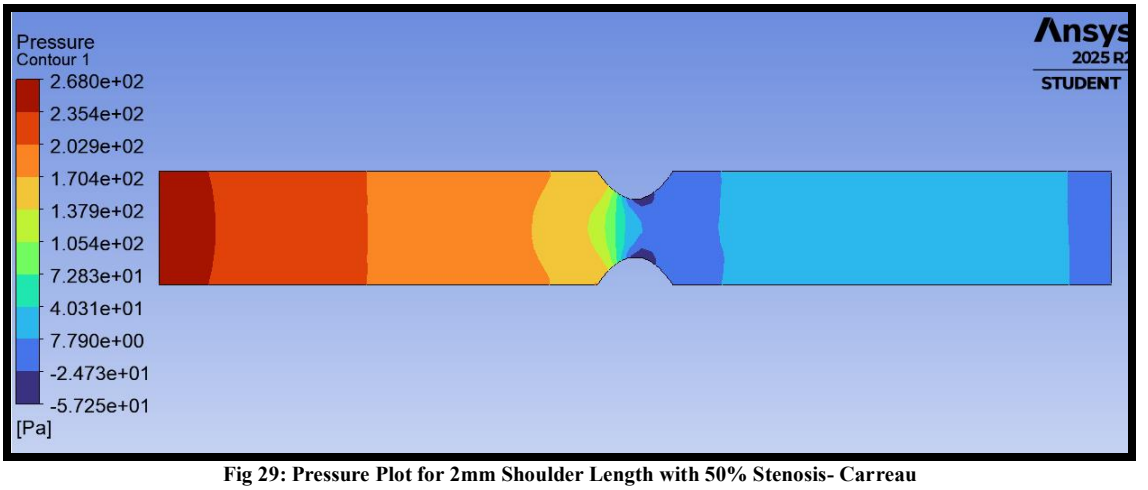

Fig 29: Pressure Plot for 2mm Shoulder Length with 50% Stenosis- Carreau

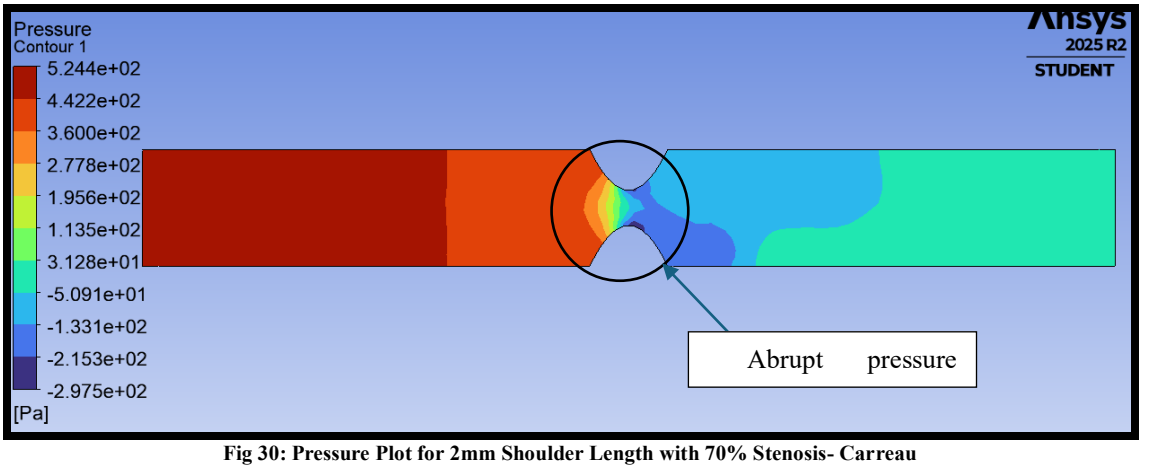

Fig 30: Pressure Plot for 2mm Shoulder Length with 70% Stenosis- Carreau

For the 2 mm shoulder length, the 30% stenosis produces a modest pressure drop across the narrowed throat, with elevated upstream pressures (red/orange) transitioning smoothly to lower downstream pressures (blue) (**Figure 28**). The short shoulder causes a relatively sharp gradient, but pressure recovery occurs quickly, reflecting the mild obstruction severity. At 50% stenosis, the pressure gradient becomes noticeably steeper, with a clear upstream–downstream contrast and reduced recovery downstream (**Figure 29**). In the most severe 70% case, a very sharp and extreme gradient is observed, with high upstream pressures (deep red) dropping abruptly to very low downstream values (blue/green) (**Figure 30**). The short 2 mm shoulder intensifies this abrupt transition, highlighting severe obstruction and substantial flow resistance compared with the 30% and 50% cases.

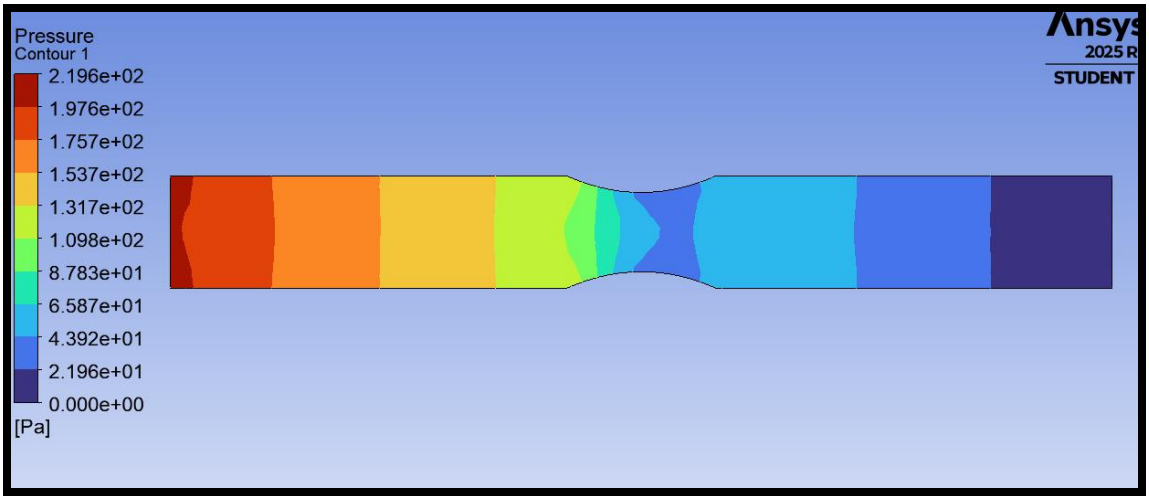

Fig 31: Pressure Plot for 4mm Shoulder Length with 30% Stenosis- Carreau

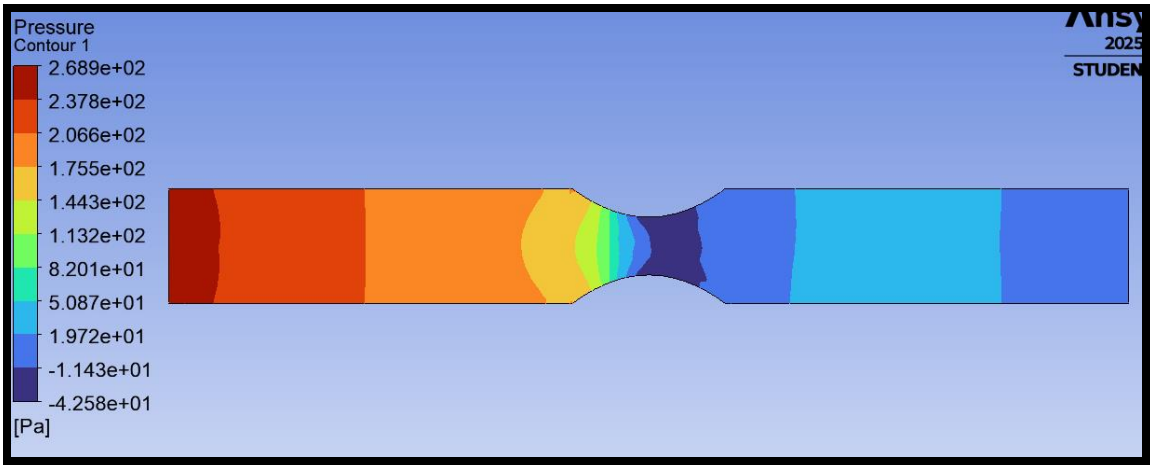

Fig 32: Pressure Plot for 4mm Shoulder Length with 50% Stenosis- Carreau

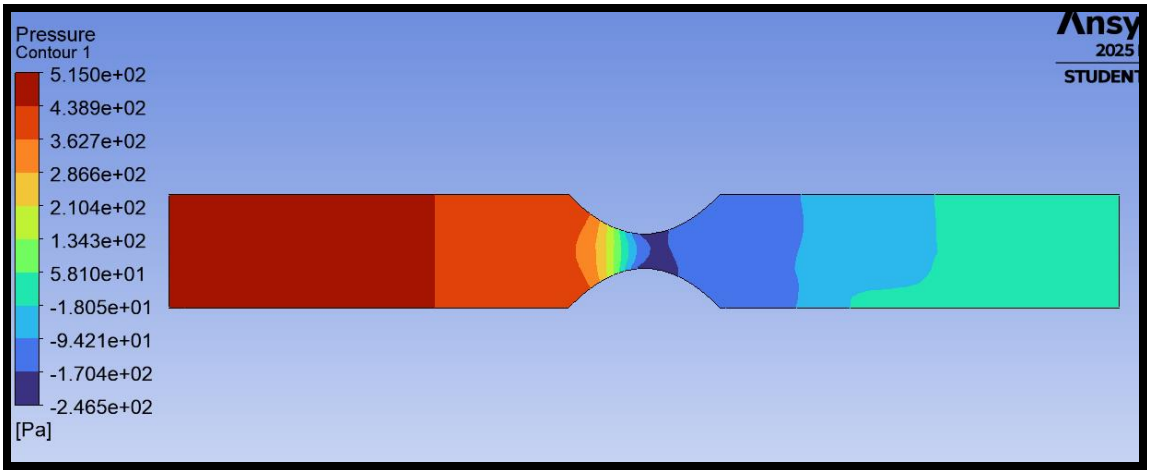

Fig 33: Pressure Plot for 4mm Shoulder Length with 70% Stenosis- Carreau

For the 4 mm shoulder length, the 30% stenosis produces a moderate pressure gradient, with a smoother transition between the upstream high-pressure region (red–orange) and reduced downstream pressure (blue–green)

(**Figure 31**). The extended shoulder reduces the sharpness of the drop compared with shorter stenoses, leading to more gradual pressure recovery and less severe flow disturbance. At 50% stenosis, the pressure gradient becomes more pronounced, with a sharper drop across the throat (**Figure 32**). While the 4 mm shoulder moderates the transition compared with the 2 mm case, downstream regions still display significant low-pressure zones (blue), reflecting higher energy loss and greater flow disturbance than in the 30% case. At 70% stenosis, a very steep pressure drop is observed, with upstream pressures exceeding 500 Pa before collapsing rapidly downstream (**Figure 33**). The longer 4 mm shoulder length smooths the gradient slightly compared with the 2 mm case, but the extended downstream low-pressure zone highlights severe energy loss and disturbed flow conditions likely to influence nanoparticle deposition.

Finally, we consider pressure evolution for the 6 mm shoulder length. In this scenario, the 30% stenosis produces a relatively small pressure drop across the throat, with upstream pressures around 220 Pa transitioning smoothly to lower downstream values (**Figure 34**). The extended shoulder further smooths the gradient compared with shorter shoulders, leading to a more evenly distributed loss and less abrupt pressure recovery. At 50% stenosis, the pressure gradient steepens, with a clear drop from approximately 280 Pa upstream to much lower values downstream of the narrowing (**Figure 35**). While the longer 6 mm shoulder moderates this transition compared with shorter cases, pressure recovery remains limited, emphasising the hemodynamic burden of increased narrowing. At 70% stenosis, the most severe changes occur, with upstream pressures exceeding 540 Pa before plunging steeply downstream of the throat (**Figure 36**). The longer shoulder length accentuates this extended high-pressure zone before the throat, followed by a sharp and sustained low-pressure region, indicating intense haemodynamic stress that could strongly influence nanoparticle deposition and plaque vulnerability.

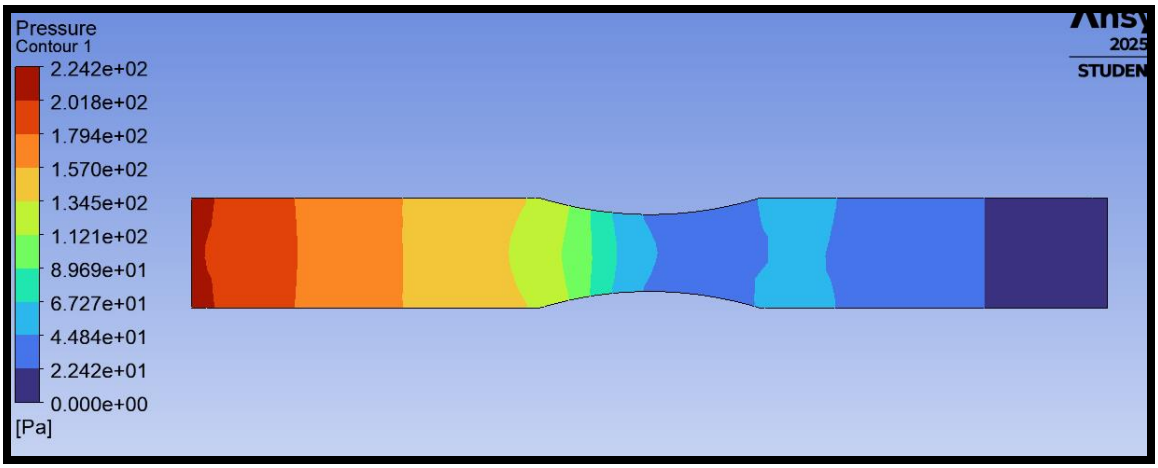

Fig 34: Pressure Plot for 6mm Shoulder Length with 30% Stenosis- Carreau

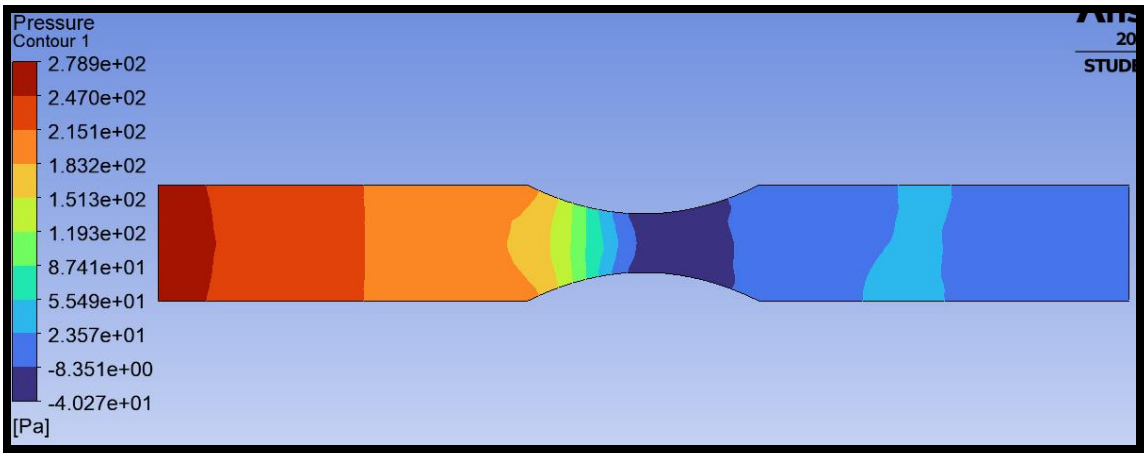

Fig 35: Pressure Plot for 6mm Shoulder Length with 50% Stenosis- Carreau

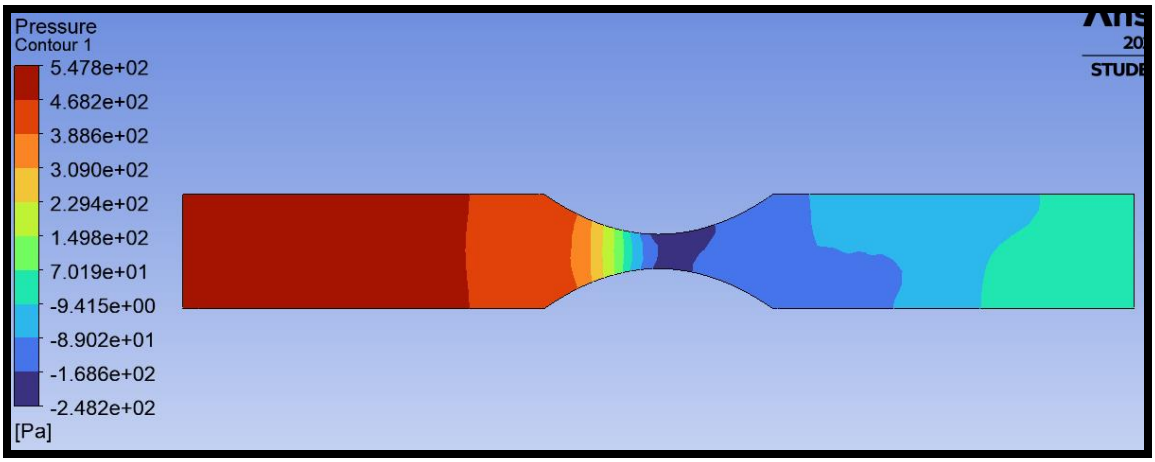

Fig 36: Pressure Plot for 6mm Shoulder Length with 70% Stenosis- Carreau

Since wall shear stress characteristics are also critical in hemodynamics, for this non-Newtonian case, we have also displayed WSS plots, which are provided in the next sub-section.

4.2.3 WSS Plots

In drug delivery applications, nano-particle deposition at plaque regions is important. We therefore analyse how stenosis depth and shoulder length influence hemodynamics at the walls of the blood vessel. Only the plaque regions are therefore displayed in the results for wall shear stresses.

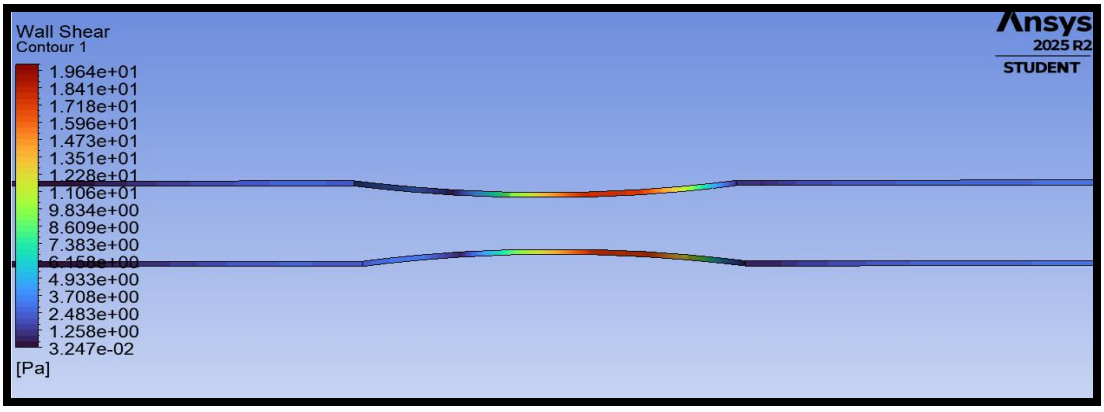

Fig 37: WSS for 2mm Shoulder Length with 30% Stenosis- Carreau

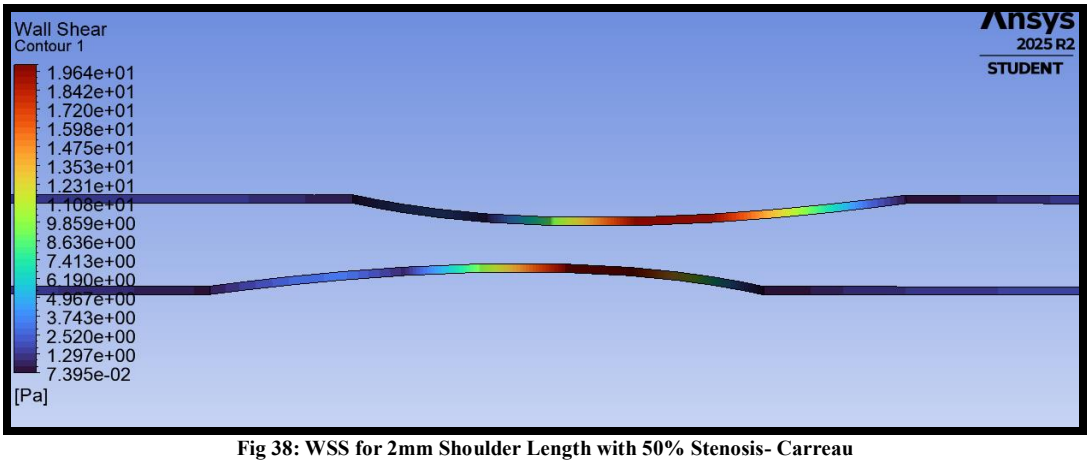

Fig 38: WSS for 2mm Shoulder Length with 50% Stenosis- Carreau

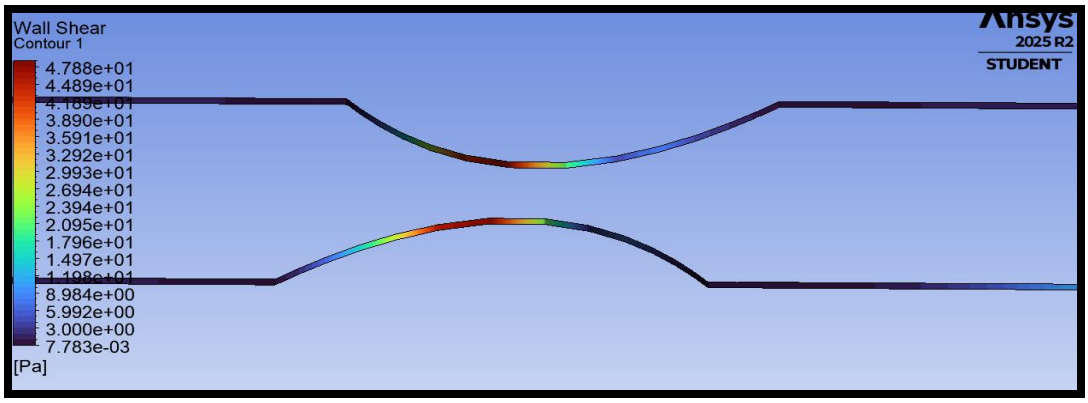

Fig 39: WSS for 2mm Shoulder Length with 70% Stenosis- Carreau

For the 2 mm shoulder length, the 30% stenosis shows a localised increase in wall shear stress (WSS) at the plaque throat, peaking around 19 Pa, while upstream and downstream values remain relatively low and uniform (**Figure 37**). This reflects a mild narrowing where elevated shear is confined to the throat and dissipates quickly, limiting nanoparticle deposition to regions of slightly elevated but stable stress. At 50% stenosis, WSS rises further, with peak stresses again approaching 19 Pa but distributed more sharply across the narrow throat (**Figure 38**). The short 2 mm shoulder produces steep gradients and concentrated high-shear zones, while downstream regions exhibit reduced WSS. At 70% stenosis, WSS reaches its highest values, exceeding 40 Pa at the throat, where the constriction generates extreme shear gradients (**Figure 39**). This strong localisation of high WSS is contrasted by reduced downstream shear, creating conditions of throat flushing and low-shear recirculation that would potentially strongly favour nanoparticle residence and deposition in drug delivery treatments (via inclusion of nanoparticle transport modelling which has been ignored in the current study) [32-34].

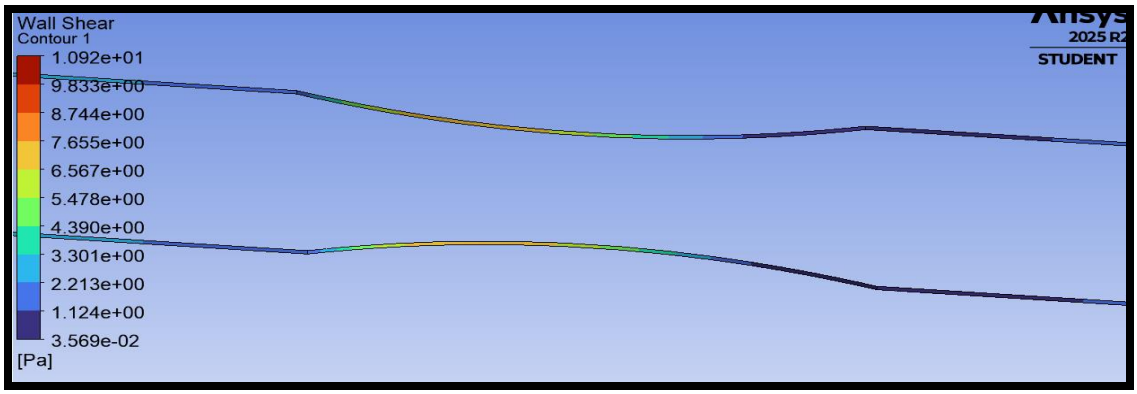

Fig 40: WSS for 4mm Shoulder Length with 30% Stenosis- Carreau

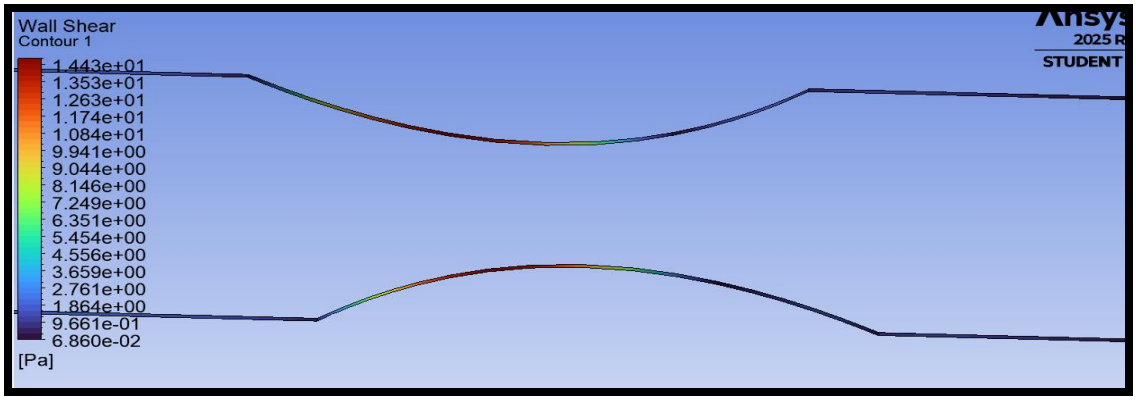

Fig 41: WSS for 4mm Shoulder Length with 50% Stenosis- Carreau

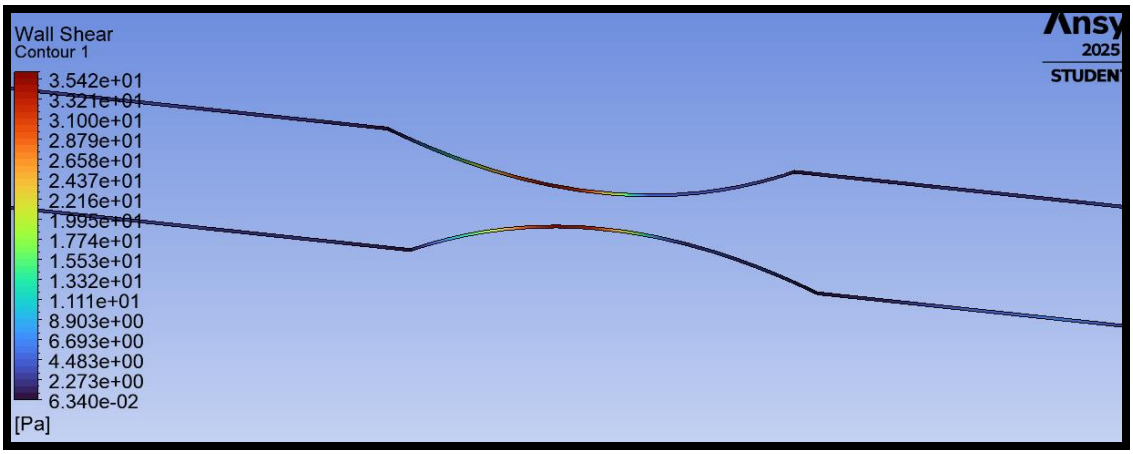

Fig 42: WSS for 4mm Shoulder Length with 70% Stenosis- Carreau

For the 4 mm shoulder length, the 30% stenosis produces relatively low WSS, peaking just above 10 Pa at the throat, with the extended shoulder smoothing the gradients and limiting recirculation downstream (**Figure 40**). At 50% stenosis, peak WSS rises above 14 Pa, concentrated at the throat but with smoother transitions into and out of the narrowing due to the longer shoulder; downstream, moderate recovery of WSS indicates disturbed regions favourable for potential nanoparticle residence (although nanoparticle simulations are not conducted here) (**Figure 41**). In the 70% stenosis case, WSS reaches its highest levels, exceeding 35 Pa at the throat, with the 4 mm shoulder producing a more gradual rise and fall compared to shorter shoulders, though the extreme narrowing still generates sharp stress concentrations strongly linked to endothelial damage and enhanced nanoparticle deposition (**Figure 42**).

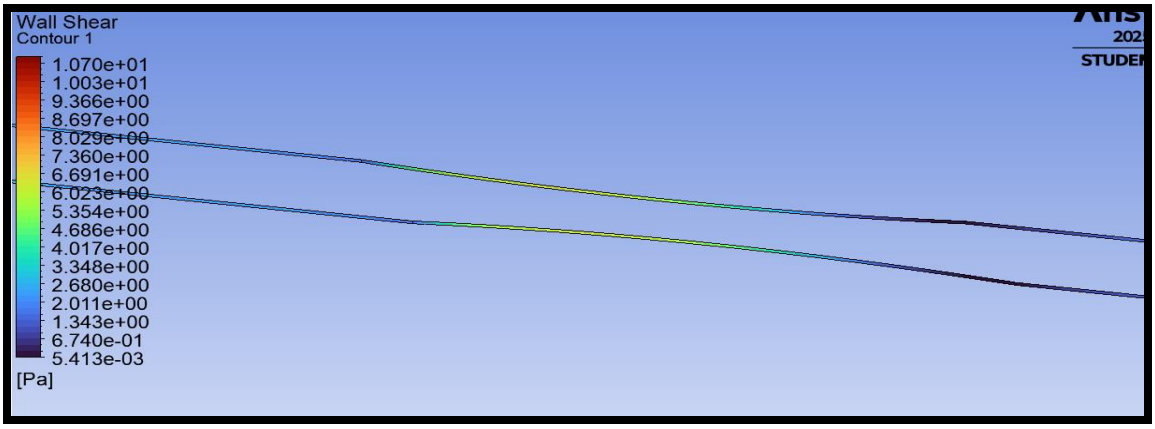

Fig 43: WSS for 6mm Shoulder Length with 30% Stenosis- Carreau

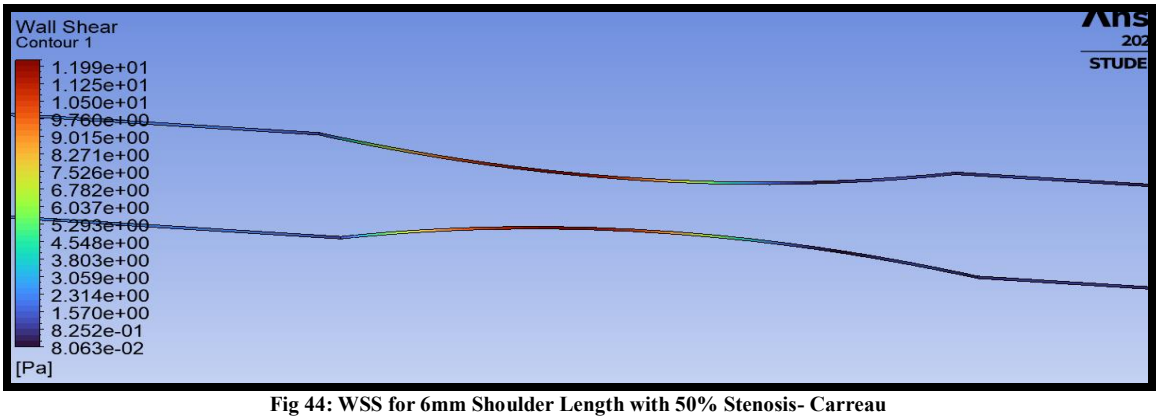

Fig 44: WSS for 6mm Shoulder Length with 50% Stenosis- Carreau

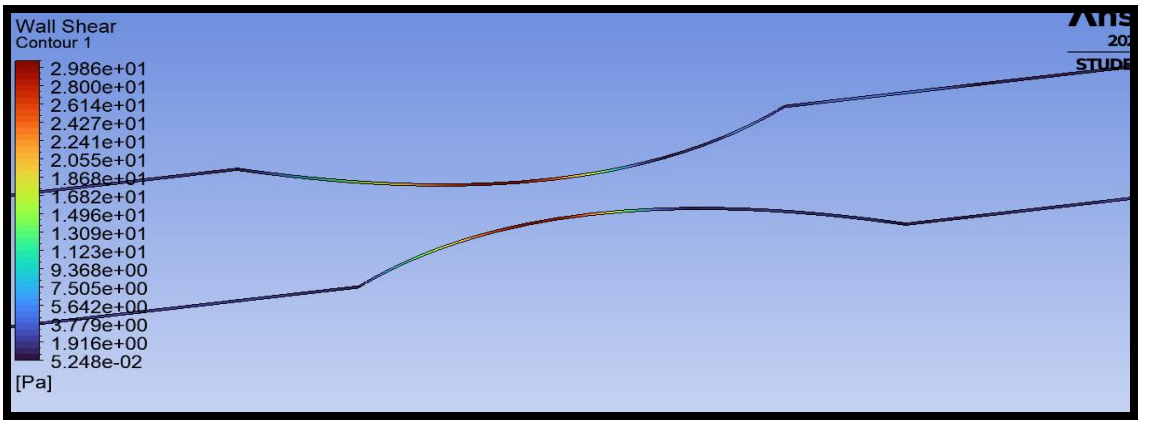

Fig 45: WSS for 6mm Shoulder Length with 70% Stenosis- Carreau

For the 6 mm shoulder length, wall shear stress (WSS) remains relatively low in the 30% stenosis case, peaking around 10 Pa at the throat, with the gradual narrowing producing smoother distributions and reduced sharp gradients compared to shorter shoulders (**Figure 43**). At 50% stenosis, WSS rises to around 12 Pa, with the extended shoulder smoothing the rise in shear but still creating stronger gradients and elevated stresses along the plaque surface (**Figure 44**). In the severe 70% stenosis case, WSS peaks close to 30 Pa at the throat, with the longer shoulder spreading the distribution more gradually, yet the extreme narrowing generates very high shear stresses strongly associated with endothelial damage and nanoparticle deposition in downstream low-shear regions (**Figure 45**).

4.1. Further Observations

4.3.1 Steady Newtonian Flow Case simulations

The steady Newtonian model represents the simplest assumption for simulating arterial blood flow, where the inlet velocity or pressure is assigned as constant and blood viscosity is assumed to remain uniform, independent of shear rate. This approach is computationally efficient and straight forward to implement from a simulation viewpoint, making it a practical starting point for analysis of this type. It is also a reasonable approximation for large arteries, where high shear rates mean blood behaves almost Newtonian as elaborated by Johnston et al. [10] and Yilmaz & Gundogdu [35].

30% Stenosis: The velocity contour plots for 30% stenosis demonstrate moderate acceleration of flow through the narrowed region, with peak velocity at the throat rising to approximately $0.3\ m/s$ which is expected at the region of stenosis in comparison to the remainder of the body where the velocity peaked at approximately $0.27\ m/s$. Flow reattaches smoothly downstream, with minimal disturbance or recirculation zones. Shorter shoulders (2 mm) generated sharper accelerations, while longer shoulders (6 mm) produced more gradual velocity transitions across the stenosis as expected. These results show that for mild stenosis, Newtonian assumptions predict relatively stable and symmetric velocity fields, consistent with expectations in large arteries where flow remains largely laminar.

50% Stenosis: For the 50% stenosis cases, the velocity profiles reveal more pronounced acceleration at the stenosis throat, with peak velocities increasing to $0.4\ m/s$ for the 2mm stenosed artery. Downstream of the constriction, the flow begins to separate, producing small but visible recirculation zones adjacent to the vessel wall which can be seen more prominently in the short and intermediate (4mm and 2mm respectively) cases. Short shoulders (2 mm) result in narrower, concentrated jets, whereas longer shoulders (6 mm) extend the disturbed regions further downstream. These observations are consistent with prior studies, which show that jet formation and flow separation become more significant with increasing stenosis severity, as emphasized by Ku [8] and Berger & Jou [6].

70% Stenosis: The 70% stenosis cases exhibit the most extreme hemodynamic changes. Velocity peaks reach their maximum values at the stenosis throat (0.5m/s), forming strong, narrow jets that extend several millimetres downstream. Large recirculation zones are visible, especially for longer shoulder lengths (6 mm), where flow disturbance persists far beyond the stenotic site. The intermediate 4 mm shoulder lengths demonstrate behaviour between these extremes, with moderate jets and recirculation lengths. These results highlight the sensitivity of downstream flow to both stenosis severity and geometric variation at the plaque shoulders, which has been highlighted among others by Mandal [17].

General Observations and Limitations: Across all cases, the steady Newtonian assumption produced smooth and symmetric velocity distributions due to the constant viscosity model. While this provides a useful baseline and is valid for large arteries where blood approximates Newtonian behaviour, it fails to capture critical physiological characteristics. Under realistic conditions, blood is pulsatile, with systolic acceleration and diastolic deceleration influencing near-wall behaviour and exhibits non-Newtonian shear-thinning properties that reduce viscosity in regions of high shear, such as near plaque surfaces as noted by Caro et al. [36]. These effects are not captured in the steady Newtonian results, meaning that important factors such as enhanced nanoparticle deposition in low-shear or oscillatory regions are underpredicted, as elucidated further by Decuzzi et al. [37].

It is also important to note that this study employs a two-dimensional model of arterial flow. While this is computationally efficient and provides insight into the key haemodynamic trends, it cannot capture out-of-plane secondary flows which are often observed in three-dimensional vessels. These secondary flows play an important role in redistributing shear stress and influencing nanoparticle trajectories, meaning the 2D results represent a simplified approximation of the real vascular environment. From the perspective of nanoparticle drug delivery, the steady Newtonian model predicts smooth flow paths, underestimating potential deposition locations associated with low-shear or recirculating regions and is often difficult to determine nano-particle behaviours as many other factors contribute towards nano-particle deposition. Consequently, this modelling approach serves primarily as a reference case against which the effects of shear-thinning (steady non-Newtonian) and pulsatility (transient Newtonian and non-Newtonian) can be evaluated.

4.3.2 Pulsatile Non-Newtonian (Carreau) Case Simulations

The pulsatile non-Newtonian Carreau model provides a realistic demonstration of arterial blood flow by incorporating shear-thinning viscosity and time-dependent inlet conditions. This combination captures the oscillatory behaviour of the cardiac cycle and the non-Newtonian rheology of blood, both of which strongly influence flow in stenosed arteries – as demonstrated also by Cho & Kensey [15] and Johnston et al. [10]. The velocity contour plots for this case illustrate how these factors interact across different stenosis severities and shoulder geometries.

4.3.2.1 *Velocity Plots*

30% Stenosis: At mild narrowing, flow acceleration through the stenosis was moderate, producing relatively smooth velocity distributions with minimal recirculation downstream. The effect of shoulder length was subtle. Short shoulders (2 mm) caused sharper acceleration, while longer shoulders (6 mm) spread the velocity increase more gradually. These patterns suggest that at low stenosis severity, flow remains relatively stable, and potential nanoparticle transport in drug treatments would primarily follow the bulk velocity profile, with limited deposition in downstream regions.

50% Stenosis: At moderate stenosis, flow disturbances became more pronounced. Peak velocities at the throat increased, and recirculation zones developed downstream of the stenosis. The 2 mm case exhibited a concentrated jet and sharp shear gradients, whereas the 6 mm case showed broader jets with extended low-velocity regions. The 4 mm case represented an intermediate behaviour. These recirculation zones are significant, as they create areas of low shear and prolonged residence time where nanoparticles may accumulate, especially during diastolic phases of pulsatile flow.

70% Stenosis: Severe stenosis cases generated the most extreme results, with very high velocity jets at the throat and large recirculation zones downstream. The short-shoulder stenosis produced a highly concentrated jet, while the long-shoulder stenosis exhibited broader jets and the largest low-velocity recirculation regions. Disturbed flow regions such as these are strongly associated with atherosclerosis progression and represent likely locations for nanoparticle deposition, particularly during low-flow phases of the pulsatile cycle when residence times increase.

General Observations and Limitations: The Carreau model moderated shear near the stenosis surfaces by reducing viscosity in high-shear regions, leading to smoother velocity gradients compared to the Newtonian case. The difference between both models is particularly important in potential applications involving predicting

nanoparticle deposition (which we did not consider here), as Newtonian models tend to overpredict wall shear stress and underestimate low-shear regions favourable to adhesion, as described by Boyd et al. [38]. While the pulsatile non-Newtonian model represents a significant step towards real life scenarios, certain simplifications remain. The model assumed axisymmetric, idealised geometries, whereas real arterial stenoses are often irregular in shape. Finally, nanoparticle dynamics were assumed from the results found rather than directly simulated, meaning particle–wall interactions and Brownian diffusion effects are not explicitly represented. These limitations highlight the need for more advanced models to fully capture the complexity of nanoparticle drug delivery in diseased arteries.

4.3.2.2 Pressure Plots

The pressure contour plots for the pulsatile non-Newtonian Carreau model show a pressure drop across the stenotic throat, with the magnitude of this drop increasing with stenosis severity.

30% Stenosis: For the 30% stenosis cases, the pressure reduction is relatively modest, with smooth gradients across the narrowing. At this relatively low stenosis, the flow remains stable, and pressure recovery occurs quickly downstream.

50% Stenosis: As stenosis increases to 50%, the pressure gradient becomes significantly steeper across the throat. The plots show clear zones of high upstream pressure and reduced downstream pressure, reflecting increased resistance to flow through the narrowed stenosed region. This sharper gradient is accompanied by stronger velocity jets in the velocity plots, indicating the close coupling between velocity acceleration and pressure reduction.

70% Stenosis: In the most severe 70% stenosis cases, the pressure drops become more pronounced, with upstream pressures rising greatly and downstream regions showing pronounced low-pressure zones. The transition across the stenotic throat is abrupt, and downstream recovery is less efficient due to flow separation and recirculation. These results align with clinical observations that pressure drops scale nonlinearly with stenosis severity, with haemodynamically significant gradients typically occurring beyond 50% narrowing.

General observations: Shoulder length also influenced the pressure distribution. Short shoulders (2 mm) produced sharper and more localised pressure drops, while longer shoulders (6 mm) spread the pressure gradient more gradually across the stenosis, reducing the abruptness of the transition but prolonging low-pressure regions downstream. The intermediate 4 mm cases again lay between these two extremes as expected. This highlights how plaque geometry, and not just severity, shapes haemodynamic stresses on the arterial wall. In relation to nanoparticle deposition in potential pharmacodynamic treatments, these pressure plots are particularly relevant. Regions of low downstream pressure, coupled with disturbed flow, are often associated with prolonged particle residence and greater likelihood of adhesion as noted in Decuzzi et al. [37] . From the pressure plots alone, the assumption could be made that nanoparticles as deployed in drug delivery, would most likely deposit in arteries where stenosis depth is greater in comparison to arteries where stenosis depth is less deep. By incorporating both pulsatile flow and non-Newtonian shear-thinning behaviour, the Carreau model provides a more accurate estimate of pressure environments than the steady Newtonian assumption in clinical scenarios.

4.3.2.3 WSS Plots

The WSS plots for the pulsatile non-Newtonian Carreau model provide crucial insight into the haemodynamic environment at the plaque surface. As expected, WSS increased at the stenotic throats due to velocity acceleration, while downstream regions exhibited lower, often oscillatory shear stresses. These patterns are directly relevant for nanoparticle adhesion and plaque vulnerability, as both low and oscillatory WSS have been linked to atherosclerosis progression.

30% Stenosis: For 30% stenosis, the WSS peaks were moderate compared to more severe cases, with relatively uniform shear across the plaque shoulders. Flow disturbance was limited, and downstream shear values quickly returned. These conditions suggest minimal chances of enhancement for nanoparticle deposition, consistent with milder obstruction where near-wall flow remains more stable.

50% Stenosis: In the 50% stenosis cases, WSS gradients became more pronounced. Peak shear stresses were observed at the throat, accompanied by sharp reductions downstream. The presence of low WSS immediately past the stenosis indicates regions of recirculation where nanoparticles are more likely to linger and adhere. The oscillatory nature of pulsatile flow further amplifies these effects, creating time-varying hotspots for particle deposition.

70% Stenosis: The most severe 70% stenosis cases demonstrated extreme WSS behaviour. Very high stresses were concentrated at the plaque throat, while downstream regions displayed extensive areas of low and near-zero WSS. This combination of extremes is particularly relevant, as elevated stresses at the throat may contribute to plaque rupture, while low oscillatory stresses downstream favour nanoparticle deposition and inflammatory processes that accelerate atherosclerosis. The influence of shoulder length was also evident, with shorter shoulders

(2 mm) producing sharper, more localised peaks in WSS, whereas longer shoulders (6 mm) distributed the stresses over a wider area but created larger low-WSS zones downstream.

General Observations: Overall, these WSS plots highlight the advantages of combining pulsatility with a non-Newtonian model. Compared with steady Newtonian assumptions, the Carreau model reduces the tendency to overpredict WSS near plaque surfaces, while pulsatile inflow captures the oscillations that are critical in nanoparticle adhesion dynamics. Observing the results from a drug delivery perspective, regions of low and oscillatory WSS identified in these simulations are potential sites for targeted nanoparticle deposition, aligning with previous experimental and computational findings including Decuzzi et al. [37].

5. Conclusions and future pathways

This study compared steady Newtonian and pulsatile non-Newtonian Carreau models to assess haemodynamics in stenosed arteries and their implications for nanoparticle deposition. In the steady Newtonian simulations, velocity plots confirmed that increasing stenosis severity (30%–70%) intensified jet velocities at the throat and extended downstream recirculation, with shoulder length influencing whether flow acceleration was sharp (short shoulders) or gradual (long shoulders). While this baseline Newtonian steady state case captured geometric influences, it neglected pulsatile and shear-thinning effects, meaning nanoparticle residence in low-shear zones was likely under-represented. In contrast, the pulsatile Carreau model provided a physiologically realistic haemo-rheological assessment of actual blood flow. Velocity plots highlighted systolic flushing and diastolic stagnation, pressure plots revealed nonlinear drops scaling with stenosis severity, and WSS plots identified high-shear throats with low or oscillatory WSS downstream. These disturbed zones correspond to predicted hotspots for nanoparticle deposition, consistent with experimental and computational evidence (e.g. see refs. [32, 37]). The results therefore confirm that stenosis severity determines the magnitude of haemodynamic disruption, while shoulder length governs its spatial distribution, jointly shaping deposition-prone regions. Increasing stenosis severity from 30% to 70% consistently elevated velocity at the stenotic throat, produced larger downstream recirculation zones, increased pressure drops, and generated extreme WSS gradients. These disturbed flow conditions correspond to regions where nanoparticles are more likely to accumulate, particularly in low- and oscillatory-WSS zones downstream of the stenosis. Shoulder length further modulated these effects: shorter shoulders (2 mm) caused sharper accelerations and highly localised shear peaks, while longer shoulders (6 mm) spread these gradients over a wider area but created extended regions of low WSS that favour particle residence and adhesion. The CFD simulations confirm that nanoparticles preferentially deposit in regions of low and oscillatory WSS, particularly downstream of severe and long shouldered stenoses, aligning with known mechanisms of atherosclerosis progression and targeted drug delivery. Future studies could extend this framework to fluid–structure interaction with compliant arterial walls, adopting robust approaches as described in Kuharat et al. [31], Holzapfel & Ogden [39]. Additionally other pathways include incorporating patient-specific geometries for clinical applicability and simulating explicit nanoparticle transport to validate deposition predictions using a variety of models such as the Buongiorno two-component nanoscale model (as studied by Tripathi et al. [40]) or the Tiwari-Das volume fraction model as considered by Dubey et al. [41] and Tripathi et al. [42]). By advancing model robustness, CFD can further support the development of nanoparticle-based targeted therapies for cardiovascular disease. Efforts in these directions are currently underway and will be reported imminently.

References

[1] W. H. Organization. *Cardiovascular diseases (CVDs)*, Accessed; https://www.who.int/news-room/fact-sheets/detail/cardiovascular-diseases-(cvds). English

[2] J. Frostegård, Immunity, atherosclerosis and cardiovascular disease, *BMC medicine,* Vol. 11, No. 1, pp. 117, 2013.

[3] D. P. Ramji, A. Ismail, J. Chen, F. Alradi, S. Al Alawi, *Survey of in vitro model systems for investigation of key cellular processes associated with atherosclerosis*, in: *Atherosclerosis: Methods and Protocols*, Eds., pp. 39-56: Springer, 2022.

[4] G. Franck, G. Even, A. Gautier, M. Salinas, A. Loste, E. Procopio, A.-T. Gaston, M. Morvan, S. Dupont, C. Deschildre, Haemodynamic stress-induced breaches of the arterial intima trigger inflammation and drive atherogenesis, *European heart journal,* Vol. 40, No. 11, pp. 928-937, 2019.

[5] M. Owais, A. Y. Usmani, K. Muralidhar, Pulsatile flow hemodynamics in stenosed arterial curvatures, *Physical Review Fluids,* Vol. 10, No. 6, pp. 063101, 2025.

[6] S. Berger, L.-D. Jou, Flows in stenotic vessels, *Annual review of fluid mechanics,* Vol. 32, No. 1, pp. 347-382, 2000.

[7] W. W. Nichols, M. O'Rourke, E. R. Edelman, C. Vlachopoulos, 2022, *McDonald's blood flow in arteries: theoretical, experimental and clinical principles*, CRC press,

[8] D. N. Ku, D. P. Giddens, C. K. Zarins, S. Glagov, Pulsatile flow and atherosclerosis in the human carotid bifurcation. Positive correlation between plaque location and low oscillating shear stress, *Arteriosclerosis: An Official Journal of the American Heart Association, Inc.,* Vol. 5, No. 3, pp. 293-302, 1985.

[9] S. S. Shibeshi, W. E. Collins, The rheology of blood flow in a branched arterial system, *Applied rheology (Lappersdorf, Germany: Online),* Vol. 15, No. 6, pp. 398, 2005.

[10] B. M. Johnston, P. R. Johnston, S. Corney, D. Kilpatrick, Non-Newtonian blood flow in human right coronary arteries: steady state simulations, *Journal of biomechanics,* Vol. 37, No. 5, pp. 709-720, 2004.

[11] P. Ballyk, D. Steinman, C. Ethier, Simulation of non-Newtonian blood flow in an end-to-side anastomosis, *Biorheology,* Vol. 31, No. 5, pp. 565-586, 1994.

[12] U. Morbiducci, D. Gallo, D. Massai, R. Ponzini, M. A. Deriu, L. Antiga, A. Redaelli, F. M. Montevecchi, On the importance of blood rheology for bulk flow in hemodynamic models of the carotid bifurcation, *Journal of biomechanics,* Vol. 44, No. 13, pp. 2427-2438, 2011.

[13] A. Zaman, N. Ali, O. Anwar Bég, Numerical simulation of unsteady micropolar hemodynamics in a tapered catheterized artery with a combination of stenosis and aneurysm, *Medical & biological engineering & computing,* Vol. 54, No. 9, pp. 1423-1436, 2016.

[14] B. Vasu, A. Dubey, O. A. Bég, R. S. R. Gorla, Micropolar pulsatile blood flow conveying nanoparticles in a stenotic tapered artery: Non-Newtonian pharmacodynamic simulation, *Computers in Biology and Medicine,* Vol. 126, pp. 104025, 2020.

[15] Y. I. Cho, K. R. Kensey, Effects of the non-Newtonian viscosity of blood on flows in a diseased arterial vessel. Part 1: Steady flows, *Biorheology,* Vol. 28, No. 3-4, pp. 241-262, 1991.

[16] E. Nader, S. Skinner, M. Romana, R. Fort, N. Lemonne, N. Guillot, A. Gauthier, S. Antoine-Jonville, C. Renoux, M.-D. Hardy-Dessources, Blood rheology: key parameters, impact on blood flow, role in sickle cell disease and effects of exercise, *Frontiers in physiology,* Vol. 10, pp. 493606, 2019.

[17] P. K. Mandal, An unsteady analysis of non-Newtonian blood flow through tapered arteries with a stenosis, *International journal of non-linear mechanics,* Vol. 40, No. 1, pp. 151-164, 2005.

[18] S. Karimi, M. Dabagh, P. Vasava, M. Dadvar, B. Dabir, P. Jalali, Effect of rheological models on the hemodynamics within human aorta: CFD study on CT image-based geometry, *Journal of Non-Newtonian Fluid Mechanics,* Vol. 207, pp. 42-52, 2014.

[19] R. B. Bird, W. E. Stewai, E. N. Lightfoot, Phenomena Second Edition, 2002.

[20] F. M. White, Fluid mechanics *Power*, 2011.

[21] A. FLUENT, ANSYS FLUENT CFD Theory Manual, *Theory Guide*, 2025.

[22] M. Khan, H. Sardar, M. M. Gulzar, A. S. Alshomrani, On multiple solutions of non-Newtonian Carreau fluid flow over an inclined shrinking sheet, *Results in physics,* Vol. 8, pp. 926-932, 2018.

[23] J. V. Soulis, T. M. Farmakis, G. D. Giannoglou, G. E. Louridas, Wall shear stress in normal left coronary artery tree, *Journal of biomechanics,* Vol. 39, No. 4, pp. 742-749, 2006.

[24] M. E. GENDY, O. A. Bég, A. Kadir, M. Islam, D. Tripathi, Computational fluid dynamics simulation and visualization of Newtonian and non-Newtonian transport in a peristaltic micro-pump, *Journal of Mechanics in Medicine and Biology,* Vol. 21, No. 08, pp. 2150058, 2021.

[25] N. Ali, Z. Asghar, M. Sajid, O. Anwar Bég, Biological interactions between Carreau fluid and microswimmers in a complex wavy canal with MHD effects, *Journal of the Brazilian Society of Mechanical Sciences and Engineering,* Vol. 41, No. 10, pp. 446, 2019.

[26] K. Mamun, M. M. Rahman, M. N. Akhter, M. Ali, Physiological non-Newtonian blood flow through single stenosed artery, in *Proceeding of,* AIP Publishing LLC, pp. 040001.

[27] A. M. Gambaruto, J. Janela, A. Moura, A. Sequeira, Shear-thinning effects of hemodynamics in patient-specific cerebral aneurysms, *Mathematical biosciences and engineering,* Vol. 10, No. 3, pp. 649-665, 2013.

[28] G. De Nisco, M. L. Rizzini, R. Verardi, C. Chiastra, A. Candreva, G. De Ferrari, F. D'Ascenzo, D. Gallo, U. Morbiducci, Modelling blood flow in coronary arteries: Newtonian or shear-thinning non-Newtonian rheology?, *Computer Methods and Programs in Biomedicine,* Vol. 242, pp. 107823, 2023.

[29] A. Sequeira, J. Janela, An overview of some mathematical models of blood rheology, *A Portrait of State-of-the-Art Research at the Technical University of Lisbon*, pp. 65-87, 2007.

[30] V. Carvalho, D. Lopes, J. Silva, H. Puga, R. A. Lima, J. C. Teixeira, S. Teixeira, *Comparison of CFD and FSI simulations of blood flow in stenotic coronary arteries*, in: *Applications of computational fluid dynamics simulation and modeling*, Eds.: IntechOpen, 2022.

[31] S. Kuharat, M. Chaudhry, O. A. Beg, T. A. Bég, Computational hemodynamic simulation of non-Newtonian fluid-structure interaction in a curved stenotic artery, *European Mechanical Science,* Vol. 8, No. 4, pp. 226-256, 2024.

[32] R. L. Hewlin Jr, M. Smith, J. P. Kizito, Computational assessment of unsteady flow effects on magnetic nanoparticle targeting efficiency in a magnetic stented carotid bifurcation artery, *Cardiovascular Engineering and Technology,* Vol. 14, No. 5, pp. 694-712, 2023.

[33] T. Matoba, J.-i. Koga, K. Nakano, K. Egashira, H. Tsutsui, Nanoparticle-mediated drug delivery system for atherosclerotic cardiovascular disease, *Journal of cardiology,* Vol. 70, No. 3, pp. 206-211, 2017.

[34] J. Tan, A. Thomas, Y. Liu, Influence of red blood cells on nanoparticle targeted delivery in microcirculation, *Soft matter,* Vol. 8, No. 6, pp. 1934-1946, 2012.

[35] F. Yilmaz, M. Y. Gundogdu, A critical review on blood flow in large arteries; relevance to blood rheology, viscosity models, and physiologic conditions, *Korea-Australia Rheology Journal,* Vol. 20, No. 4, pp. 197-211, 2008.

[36] C. G. Caro, 2012, *The mechanics of the circulation*, Cambridge University Press,

[37] P. Decuzzi, S. Lee, B. Bhushan, M. Ferrari, A theoretical model for the margination of particles within blood vessels, *Annals of biomedical engineering,* Vol. 33, No. 2, pp. 179-190, 2005.

[38] J. Boyd, J. M. Buick, S. Green, Analysis of the Casson and Carreau-Yasuda non-Newtonian blood models in steady and oscillatory flows using the lattice Boltzmann method, *Physics of Fluids,* Vol. 19, No. 9, 2007.

[39] G. A. Holzapfel, R. W. Ogden, 2003, *Biomechanics of soft tissue in cardiovascular systems*, Springer Science & Business Media,

[40] J. Tripathi, B. Vasu, O. A. Bég, R. S. R. Gorla, Unsteady hybrid nanoparticle-mediated magneto-hemodynamics and heat transfer through an overlapped stenotic artery: Biomedical drug delivery simulation, *Proceedings of the Institution of Mechanical Engineers, Part H: Journal of Engineering in Medicine,* Vol. 235, No. 10, pp. 1175-1196, 2021.

[41] A. Dubey, B. Vasu, O. Anwar Bég, R. S. Gorla, A. Kadir, Computational fluid dynamic simulation of two-fluid non-Newtonian nanohemodynamics through a diseased artery with a stenosis and aneurysm, *Computer Methods in Biomechanics and Biomedical Engineering,* Vol. 23, No. 8, pp. 345-371, 2020.

[42] J. Tripathi, B. Vasu, O. A. Bég, Computational simulations of hybrid mediated nano-hemodynamics (Ag-Au/Blood) through an irregular symmetric stenosis, *Computers in Biology and Medicine,* Vol. 130, pp. 104213, 2021.